



1

2

3

4

## **New particle formation in the Svalbard region 2006 - 2015**

5

6

Jost Heintzenberg<sup>1</sup>, Peter Tunved<sup>2</sup>, Martí Galí<sup>3</sup>, and Caroline Leck<sup>4</sup>

7

8

9

1: Leibniz Institute for Tropospheric Research (TROPOS), Permoserstr. 15, 04318 Leipzig,

10

Germany

11

2: Department of Applied Environmental Science, Stockholm University (MISU), 10691

12

Stockholm, Sweden

13

3: Takuvik Joint International Laboratory & Québec-Océan, Université Laval, G1V 0A6

14

Québec, Canada

15

4: Department of Meteorology, Stockholm University (MISU), 10691 Stockholm, Sweden

16



17 Abstract

18

19 Events of new particle formation, (NPF), were analyzed in a ten-year data set of hourly  
20 particle size distributions recorded on Mt. Zeppelin, Spitsbergen, Svalbard. Three different  
21 types of NPF-events were identified through objective search algorithms. The first and  
22 simplest algorithm utilizes short-term increases in particle concentrations below 25 nm,  
23 (PCT-events). The second one builds on the growth of the sub-50 nm diameter-median,  
24 (DGR-events), and is most closely related to the classical “banana-type” of events. The third  
25 and most complex, so-called multiple-size approach to identifying NPF-events builds on a  
26 hypothesis suggesting the concurrent production of polymer gel particles at several sizes  
27 below about 60 nm, (MEV-events).

28 As a first and general conclusion we can state that NPF-events are a summer phenomenon  
29 and not related to Arctic haze, which is a late winter-to-early spring event. NPF-events  
30 appear to be somewhat sensitive to the available data on precipitation. The seasonal  
31 distribution of solar flux suggests some photochemical control that may affect marine  
32 biological processes generating particle precursors and/or atmospheric photochemical  
33 processes that generate condensable vapors from precursor gases. Whereas the seasonal  
34 distribution of the biogenic methanesulfonate, (MSA), follows that of the solar flux it peaks  
35 before the maxima in NPF-occurrence.

36 A host of ancillary data and findings point to varying and rather complex marine biological  
37 source processes. The potential source regions for all types of new particle formation appear  
38 to be restricted to the marginal ice and open water areas between Northeastern Greenland and  
39 Eastern Svalbard. Depending on conditions yet to be clarified new particle formation may  
40 become visible as short bursts of particles around 20 nm, (PCT-events), longer events  
41 involving condensation growth, (DGR-events), or extended events with elevated  
42 concentrations of particles at several sizes below 100 nm, (MEV-events). The seasonal



43 distribution of NPF-events peaks later than that of MSA and, DGR and in particular of MEV-  
44 events reach into late summer and early fall with much open, warm, and biologically active  
45 waters around Svalbard. Consequently, a simple model to describe the seasonal distribution  
46 of the total number of NPF-events can be based on solar flux, and sea surface temperature,  
47 representing environmental conditions for marine biological activity, and condensation sink,  
48 controlling the balance between new particle nucleation and their condensational growth.  
49 Based on the sparse knowledge about the seasonal cycle of gel-forming marine  
50 microorganisms and their controlling factors we hypothesize that the seasonal distribution of  
51 DGR and more so MEV-events reflect the seasonal cycle of the gel-forming phytoplankton.

52

53



## 54 1. Introduction

55

56 In the late 1970ies and early 1980ies the interest in the Arctic atmospheric aerosol widened  
57 from the well-identified winter phenomenon of Arctic haze (Rahn and Shaw, 1977;  
58 Heintzenberg and Leck, 1994) to summer conditions in this northernmost remote region. In  
59 the pristine Arctic summer air the so-called background aerosol (Junge, 1963) was expected  
60 to be most clearly visible, far away from the northern hemispheric anthropogenic emission  
61 centers at lower latitudes. Episodic and localized occurrences of high concentrations of  
62 ultrafine particles, (here defined as particles with diameters  $< 100$  nm), in the summer Arctic  
63 were explained by rare import of polluted air from lower latitudes (Flyger and Heidam, 1978;  
64 Heintzenberg and Larssen, 1983) or hypothetical anthropogenic sources in the Arctic  
65 (Jaenicke and Schütz, 1982).

66 With the advent of sensitive condensation nuclei counters (Agarwal and Sem, 1980) and  
67 differential mobility analyzers (Knutson and Whitby, 1975a, b) more details became visible in  
68 the Arctic sub-micrometer aerosol. High numbers of ultrafine particles were observed in  
69 connection with fog passages (Lannefors et al., 1983) and chemical aerosol information  
70 indicated a regional – possibly biogenic – particle sources in the summer Arctic  
71 (Heintzenberg, 1989). The high molar ratios of methane sulfonate, (MSA), to non-sea salt  
72 sulfate, ( $\text{nssSO}_4^{2-}$ ), of 0.28 in the Arctic summer aerosol found by Heintzenberg and Leck  
73 (1994) substantiated the biogenic source of the particles.

74 The establishment of long-term Arctic aerosol monitoring at the fringes of the pack ice in  
75 Alaska (e.g., Polissar et al., 1999), Canada (e.g., Norman et al., 1999; Willis et al., 2016), and  
76 on Spitsbergen (e.g., Tunved et al., 2013) revealed more details of potential sources of the  
77 summer aerosol, in particular their connection to the marine biosphere in the Arctic. The  
78 unique series of systematic aerosol studies in the central Arctic north of  $80^\circ\text{N}$  onboard the  
79 Swedish icebreaker *Oden* in 1996 led to the formulation of a new hypothesis concerning a



80 specific process of marine biogenic particle formation (Leck and Bigg, 1999). The marine  
81 biogenic particles involved behaved as polymer gels and originated in the surface microlayer  
82 (SML) of the ocean, (Orellana et al., 2011b), from the activity of sea-ice algae,  
83 phytoplankton and, perhaps, bacteria. The new particle events were reported to occur as  
84 simultaneous enhancement of particle number concentrations in the whole size-range below  
85 50 nm, and not with the prototypical “banana growth” (Kulmala et al., 2004). Two more  
86 *Oden* cruises in 2001 and 2008 yielded results that were partly contradicting (Held et al.,  
87 2011b; Held et al., 2011a), partly supporting the SML hypothesis (Leck et al., 2013; Karl et  
88 al., 2013; Orellana et al., 2011b; Leck and Bigg, 2010). The synopsis of the results of four  
89 *Oden* cruises of Heintzenberg et al. (2015) identified geographic regions of new particle  
90 formation (NPF) in the inner Arctic while stressing the importance of recent open water and  
91 related biological activity in the sea in transects by air masses with new particle formation  
92 over the central Arctic.

93 Two years of aerosol size distributions from Mt. Zeppelin, Spitsbergen and Alert, both  
94 located at the fringes of the central pack ice, were analyzed by Croft et al. (2016a) with a  
95 global aerosol geophysics model. They discuss classical new-particle nucleation, coagulation  
96 scavenging in clouds, scavenging by precipitation, and transport in order to explain the annual  
97 cycle of the Arctic aerosol. Croft et al. (2016a) find two seasonal maxima in their modeled  
98 particle nucleation rates, one in March, and one in July. In spring, their simulated NPF occurs  
99 mainly in the free troposphere, whereas in summer, it occurs also in the planetary boundary  
100 layer. More recently, Croft et al. (2016b) state that ammonia from seabird-colony guano is a  
101 key factor contributing to bursts of newly formed particles, which are observed every summer  
102 in the near-surface atmosphere, at least at Alert, Nunavut, Canada. Earlier, the results of  
103 studies with another global aerosol model by Browse et al. (2014) suggested that the potential  
104 increase in NPF in the Arctic with potential increases in cloud condensation nuclei is



105 compensated by wet scavenging. They also state that scavenging by pre-existing large  
106 particles suppresses NPF-events.

107 Based on three years of data from the two Arctic sites Thule and Ny-Ålesund (gruvebadet)  
108 Becagli et al. (2016) examined the sources and environmental factors controlling the  
109 biological aerosol component MSA. Their analysis included satellite-derived Chlorophyll-*a*  
110 (an indicator of phytoplankton biomass), oceanic phytoplankton primary productivity, (PPP),  
111 and sea ice. Whereas they found good correlations between MSA, PPP and sea ice, (the latter  
112 two being closely related), their data did not allow any statements on NPF processes.

113 To date the longest record of sub-micrometer number-size distributions of the Arctic  
114 aerosol down to 5 nm particle diameter and below has been accumulated on Mt. Zeppelin,  
115 Spitsbergen (Tunved et al., 2013; Heintzenberg and Leck, 1994). For the ten years from 2006  
116 through 2015 a total of 63936 quality-controlled hours of aerosol data are available, i.e.  
117 during 73% of all hours of the ten years. In the present study we exploit this formidable data  
118 set in a search for processes forming new particles. An important first step in this work was  
119 formulating completely objective criteria for the identification of events. In the relatively  
120 clean Arctic environment we do not expect the classical nucleation and growth events as  
121 frequently observed over the continents, (cf. Kulmala et al., 2004), to dominate. Thus, we  
122 refrained from applying the objective search algorithm formulated by Heintzenberg et al.,  
123 (2007) for this “Banana-type” of events. Instead we formulated new objective search  
124 algorithms allowing several potential types of new particle formation events or formation  
125 processes. With a host of complementary atmospheric and surface physical, chemical, and  
126 biological information a large number of NPF-events identified with these algorithms will be  
127 analyzed in the following chapters.

128

129

130



131 **2. Database**

132

133 The Mt. Zeppelin observatory

134

135 Situated at the top of Mt Zeppelin, Svalbard (78° 56'N, 11° 53'E), the Zeppelin observatory

136 offers a unique possibility to study the characteristic features of Arctic atmospheric

137 constituents such as trace gases and aerosol particles. At a height of 474 m a.s.l. the station is

138 located near the top of the local planetary boundary layer and represents remote Arctic

139 conditions. The closest source of pollution, the small community of Ny-Ålesund, is located

140 ~2 km north of the station

141 ([http://www.esrl.noaa.gov/psd/iasoa/sites/default/files/stations/nyalesund/nyalesund\\_site.jpg](http://www.esrl.noaa.gov/psd/iasoa/sites/default/files/stations/nyalesund/nyalesund_site.jpg)).

142 However, the elevation difference and typical wind patterns largely prevent pollution from

143 nearby sources to reach the Zeppelin Observatory. The dominating wind pattern is east-

144 southeast katabatic flow from Kongsvegen glacier or from northwesterly directions as

145 channeled by the Kongsfjord (Beine et al., 2001; Heintzenberg et al., 1983). The station itself

146 was initially established in 1991, and is owned by the Norwegian Polar Research Institute

147 (NP). The Norwegian Institute for Air Research (NILU) is responsible for the coordination of

148 the scientific program.

149

150

151 **2.1 Physical aerosol data**

152

153 After a period of continuous aerosol measurements by the Department of Meteorology,

154 Stockholm University in the early 1990ties, (Heintzenberg and Leck, 1994), the Department

155 of Analytical Chemistry and Environmental Science, Stockholm University, initialized

156 observations of the aerosol number size distribution in mid-2000. Originally, the system



157 consisted of a single differential mobility analyzer system, (DMPS), consisting of a medium-  
158 size Hauke-type differential mobility analyzer, (DMA), together with a TSI 3760  
159 condensation particle counter, covering diameters between 20 and ~500nm. From 2006 on  
160 the particle size range was widened covering particle sizes between 10 and 790 nm. In 2005,  
161 the rain-cover over the inlet was replaced. Initially, the instrument inlet was of a PM10 type,  
162 removing particles or hydrometeors with diameters  $>10\ \mu\text{m}$  from the sampled air stream.  
163 During a substantial renewal of the Stockholm University equipment in 2010-2011, both inlet  
164 and DMPS system were replaced.

165 Since then, the DMPS-system utilizes a custom-built twin DMA-setup comprising one  
166 Vienna-type medium DMA coupled to a TSI CPC 3010 covering sizes between 25-800 nm  
167 and a Vienna-type long DMA coupled with at TSI CPC 3772 covering sizes between 5-60  
168 nm. The size distributions from the two systems are harmonized on a common size grid and  
169 then merged. Both systems use a closed-loop flow setup. The current inlet hat is of whole air  
170 type, complying with EUSAAR<sup>1</sup> standard for high altitude or Arctic sampling conditions. In  
171 the current setup, the inlet is operated with a flow of ca. 100 liters per minute, (lpm). Laminar  
172 flow conditions apply throughout the sampling lines. Outside of the station, the inlet  
173 temperature is kept above 0°C using active heating. Inside the station the temperature  
174 increases gradually to room temperature (maximum temperature reaches ca. 25 °C, but  
175 remains typically around 20°C). Relative humidity, (RH) and temperature are internally  
176 monitored and measurements are maintained at dry conditions with  $\text{RH} < 30\%$ . The system is  
177 regularly checked with latex spheres and flow controls. The recorded data are manually  
178 screened and crosschecked with other available observation as in Tunved et al. (2013). If  
179 inconsistencies were found between the different datasets, further investigation was

---

<sup>1</sup> EUSAAR (European Supersites for Atmospheric Aerosol Research) is an EU-funded I3 (Integrated Infrastructures Initiatives) project carried out in the FP6 framework of the specific research and technological development program "Structuring the European Research Area - Support for Research Infrastructures", (<http://www.eusaar.net/>).



180 performed to exclude data that were identified as affected by instrumental errors. Using the  
181 instrumental logbook, periods of local activity potentially influencing the sampling were also  
182 excluded from the dataset. During the years 2006 – 2010 no particles below ten nanometers  
183 in diameter were recorded. From 2011 on four more diameter bins down to 5 nm were  
184 included and a different diameter array was utilized. To allow for a synopsis of all years all  
185 size distributions were interpolated on the pre-2011 diameter array and all integrals of the size  
186 distribution over particle diameter were taken over the joint diameter range 10 to 631 nm. For  
187 the pre-2011 years the data at the four size channels below 10 nm were flagged as missing.  
188 However, whenever results cover the complete time series the resulting number  
189 concentrations in the four first channels covering the years 2011 – 2015 are carried along.

190 For the identification of NPF in terms of particle growth the parameter D50 in nanometer  
191 was calculated as the number median diameter of particles smaller than 50 nm but larger than  
192 10 nm, i.e. 50% of all particles below that size are smaller than D50. Besides this parameter  
193 Table 1 lists nine integral particle parameters, which are utilized in the NPF-search  
194 approaches or in the interpretation of results. These aerosol parameters quantify total particle  
195 number, (NTO), and particle numbers in sub-ranges of the number size distribution such as  
196 N25, quantifying the total number of particles between ten and 25 nm.

197 Following the concept developed by Pirjola et al., (1999), and Kulmala et al., (2001) we  
198 calculated the condensation sink, (CS,  $s^{-1}$ ), as a parameter with which the probability of new  
199 particle formation from the gas phase and the necessary amount of condensable vapor can be  
200 estimated. For this calculation we utilized from our database number size distributions,  
201 pressure and temperature.

202

203

204

205

206 **2.2 Chemical aerosol data**

207

208 For the interpretation of NPF-events we employed chemical information derived from the  
209 analyses of high volume particle samples taken by the Norwegian Institute for Air research,  
210 (NILU). A high volume sampler (PM10) was used to collect samples for a quantitative  
211 determination of sodium, ( $\text{Na}^+$ ) sulfate, ( $\text{SO}_4^{2-}$ ) and MSA ( $\text{CH}_3\text{SOO}^-$ ). The sampler collected  
212 material for analysis in one to three days. Blank samples were obtained by mounting the  
213 glass fiber filters at the sampling site with the same sampling period but without air passing  
214 through.  $\text{Na}^+$  and  $\text{SO}_4^{2-}$  were analyzed by NILU and have been downloaded for the present  
215 study from the EBAS database (<http://ebas.nilu.no>), which list details about the sampling  
216 technique and the sampling protocol. To be able to apportion the measured sulfate to  
217  $\text{nssSO}_4^{2-}$  the observed concentrations of  $\text{Na}^+$  were used as the reference element based on the  
218 assuming that all  $\text{Na}^+$  is of marine origin, (Keene et al., 1986).

219 MSA was analyzed at the laboratory of the Department of Meteorology, Stockholm  
220 University. To allow for subsequent chemical determinations the ambient samples and blanks  
221 were carefully handled in a glove box (free from particles, sulfur dioxide and ammonia). At  
222 the time of the chemical analyses, still in the glove box, the substrates were extracted (in  
223 centrifuge tubes) with  $60 \text{ cm}^3$  deionized water (Millipore Alpha-Q, conductivity  $18 \text{ M}\Omega\text{cm}$ ).  
224 The extracts were thereafter analyzed for weak anions by chemically suppressed ion  
225 chromatography (IC, Dionex ICS-2000) using Dionex AG11/AS11 columns. In order to trap  
226 carbonates and other ionic contaminants a Dionex ATC-1 column was used before the  
227 injection valve. The injection volume was  $50 \mu\text{dm}^3$ . Quality checks of the IC-analyses were  
228 performed with both internal and external reference samples (Das et al., 2011). The analytical  
229 detection limits obtained for the various ions, defined as twice the level of peak-to-peak  
230 instrument noise, was  $0.0001 \mu\text{eq dm}^{-3}$  for MSA. The overall analytical accuracy was better  
231 than 1.5%.



### 232 **2.3 Back-trajectories and meteorological data**

233

234 For every hour during the ten years 2006 through 2015 three-dimensional back trajectories  
235 have been calculated arriving at 474 m at Mt. Zeppelin. The trajectories have been calculated  
236 backward for up to ten days using the HYSPLIT4 model (Draxler and Rolph, 2003) with  
237 meteorological data from the Global Data Assimilation System with one-degree resolution  
238 (GDAS1). More information about the GDAS dataset can be found at Air Resources  
239 Laboratory (ARL), NOAA (<http://ready.arl.noaa.gov>), from which the meteorological data  
240 were downloaded.

241 During the analyzed time period meteorological records at the Mt. Zeppelin station are  
242 rather limited in quality and were frequently interrupted. In order to have an internally  
243 consistent, and unbroken meteorological record we utilized the hourly meteorological  
244 parameters at trajectory arrival times as calculated by the HYSPLIT4 model. As an additional  
245 parameter we evaluated the vertical air movement of the trajectories during the last hour  
246 before arrival by subtracting the trajectory height one hour before arrival at the arrival height  
247 of 474 meter. The resulting vertical displacement parameter, DZ, is given in meters per hour.  
248 Positive values of DZ indicate a lifting of the air.

249 The most important missing meteorological information concerns the local cloudiness. No  
250 direct recording was available of times during which the station was in clouds. The closest  
251 available cloud instrument is a ceilometer operated by the Alfred Wegener Institute (AWI) at  
252 their Koldewey Station in Ny-Ålesund, i.e. in the valley below Mt. Zeppelin, some 2.8 km of  
253 horizontal distance from the position of the mountain station. From the one-minute records of  
254 the ceilometer we derived hourly values of the 25% percentile of cloud base, which was used  
255 as an indicator for the Zeppelin station being in clouds. The meteorological parameters are  
256 listed in Table 1.



257 Precipitating clouds scavenge the planetary boundary layer and thus reduce the available  
258 particle surface for condensational uptake of particle precursors. As a consequence  
259 nucleation from the gas phase may be facilitated (Tunved et al., 2013). As in Tunved et al.  
260 (2013) we utilized the HYSPLIT-modeled precipitation along the back trajectories. Sums of  
261 precipitation, (SP, see Table 1), were calculated along each back trajectory and will be  
262 referred to as SP1 (during the last day), SP2 (during the last but one day), and SP5 (during  
263 days three to five) before arrival at Mt. Zeppelin.

264

265

#### 266 **2.4 Marine biological data**

267

268 The biologically active marginal ice zone is a major natural source of sulfur in the Arctic  
269 summer atmosphere, (Leck and Persson, 1996b, a), and Wiedensohler et al. (1996), indicated  
270 a potentially important role of dimethyl sulfide (DMS) in regional new particle formation.  
271 DMS emissions from the sea have long been proposed to control new particle formation in the  
272 marine boundary layer, (Charlson et al., 1987), which builds on  $\text{DMS}_{\text{aq}}$  being transported via  
273 turbulence and diffusion to the sea-air interface, represented by the transfer velocity, which in  
274 turn depends on sea-surface temperature, salinity, and wind speed, (Liss and Merlivat, 1986).  
275 Once ventilated to the atmosphere  $\text{DMS}_{\text{g}}$  is photochemical oxidized via intermediates such as  
276 sulfuric acid and methane sulfonic acid, (Ayers et al., 1996), which eventually leads to the  
277 formation of aerosol  $\text{nssSO}_4^{2-}$  and MSA.

278 Dimethyl sulfide in the ocean ( $\text{DMS}_{\text{aq}}$ ) is produced through the degradation of its algal  
279 precursor dimethylsulfoniopropionate (DMSP) by microbial food webs, (Simó, 2001). At  
280 high latitudes, total DMSP ( $\text{DMSP}_{\text{t}}$ ) and therefore  $\text{DMS}_{\text{aq}}$ , essentially follows the seasonal  
281 cycle of phytoplankton biomass, (Lana et al., 2012).  $\text{DMSP}_{\text{t}}$  is defined as the sum of  
282  $\text{DMSP}_{\text{dissolved}}$  and  $\text{DMSP}_{\text{particulate}}$  concentration. Yet, the amount of  $\text{DMSP}_{\text{t}}$  per unit



283 phytoplankton biomass may vary depending on species composition and physiological state,  
284 (Keller et al., 1989).

285 The dissolved organic carbon (DOC) concentrations in surface waters of the high Arctic  
286 Ocean are up to ten times higher than in any other ocean basin and closer in range to DOC  
287 levels reported for sea ice (Gao et al., 2012). A large fraction of DOC spontaneously  
288 assembles into polymer gels: polysaccharide forming hydrated calcium bonded three-  
289 dimensional networks to which other organic compounds, such as proteins and lipids, are  
290 readily bound. The assembly and dispersion of the polysaccharide molecules can be affected  
291 by environmental parameters, such as UV-B radiation (280-320nm) dispersing or inhibiting  
292 gel formation, and/or pH and temperature inducing gel volume phase changes (swelling and  
293 shrinkage). In the study of Orellana et al., (2011b), the swelling and shrinking of the  
294 polysaccharide networks or polymer gels were also causally related by additions of nano to  
295 micromolar levels of DMS and DMSP. High DMSP concentrations have also been measured  
296 in the mucilage surrounding prymnesiophyte *Phaeocystis pouchetii* colonies in Arctic waters,  
297 representing up to 25% of the total water column DMSP pool, (Matrai and Vernet, 1997).

298 The findings made by Orellana et al., (2011b) were in agreement with previous findings by  
299 Orellana et al., (2011a) that high concentrations of DMSP and DMS are stored in the acidic  
300 secretory vesicles of the *Phaeocystis* algae where DMSP is trapped within the condensed  
301 polyanionic gel matrix until the secretory vesicles are triggered by environmental factors such  
302 as temperature to release gels that undergo volume phase transition and expand at the higher  
303 pH of seawater. Exocytosis of polymer gels accompanied by elevated DMS and DMSP  
304 concentrations suggests the transport of these chemical compounds by the gel matrix.  
305 Schoemann et al., (2005) report that *Phaeocystis antarctica* is particularly well adapted to low  
306 temperatures, being more competitive than *P. pouchetii* for temperatures between -2 and  
307 +2 °C. *Phaeocystis pouchetii*, however, appears to be better adapted to temperatures closer to



308 5 °C. In the Arctic a higher occurrence of the *Phaeocystis pouchetii* would be expected in the  
309 northward advection of warm Atlantic water masses around Svalbard.

310 Here we estimated DMS<sub>Pt</sub> at the sea surface using the algorithm described by Galí et al.  
311 (2015). The DMS<sub>Pt</sub> algorithm exploits the distinct relationship between DMS<sub>Pt</sub> and  
312 Chlorophyll-*a* depending on the light exposure regime of the phytoplankton community. The  
313 light exposure regime is defined by the ratio between euphotic layer depth and mixed layer  
314 depth ( $Z_{eu}/MLD$ ). Additional predictor variables used are sea surface temperature (SST) and  
315 particulate inorganic carbon (PIC), which is used in the algorithm as a proxy for  
316 coccolithophores such as *Emiliana huxleyi*. During late bloom stages, the calcite plates that  
317 cover coccolithophore cells (called coccoliths) detach and cause an increase in seawater  
318 backscatter that invalidates satellite retrievals of Chlorophyll-*a*. Therefore, inclusion of PIC  
319 in the algorithm as a proxy for DMS<sub>Pt</sub> increases data coverage. Although the algorithm was  
320 developed for the global ocean, validation results with in situ data indicate that it performs as  
321 well or slightly better in Arctic and sub-Arctic waters.

322 The use of remotely sensed DMS<sub>Pt</sub> as a proxy for marine DMS<sub>aq</sub> emission is a significant  
323 improvement with respect to prior studies that used Chlorophyll-*a* (Becagli et al., 2016;  
324 Zhang et al., 2015). Yet, it is not ideal because (i) the ratios DMS<sub>aq</sub>/DMS<sub>Pt</sub> in surface  
325 seawater are variable, and tend to be higher in high solar irradiance and nutrient-poor  
326 conditions typical of summer, (Galí and Simó, 2015), and (ii) even if DMS<sub>Pt</sub> is a better proxy  
327 for DMS<sub>aq</sub>, the influence of meteorological and sea surface conditions (mainly wind speed  
328 and SST) on the sea-air flux of DMS<sub>aq</sub> is not taken into account. Development is underway of  
329 an algorithm for the retrieval of DMS<sub>g</sub> concentrations in air and DMS fluxes.

330 The DMS<sub>Pt</sub> algorithm was run for the 2006-2015 period using daily composites of the  
331 Moderate Resolution Imaging Spectroradiometer on the Aqua satellite (MODIS-Aqua) at 4.64  
332 km resolution (L3BIN, reprocessing R2014.0) downloaded from NASA's Ocean Color  
333 website (<http://oceancolor.gsfc.nasa.gov>). The MODIS variables used include Chlorophyll-*a*



334 concentration derived with the GSM algorithm, (Maritorena et al., 2002), PIC, nighttime SST  
335 and  $Z_{eu}$ . MODIS nighttime SST was complemented with SST from the Advanced Very High  
336 Resolution Radiometer (AVHRR, <https://podaac.jpl.nasa.gov/AVHRR-Pathfinder>) to increase  
337 data availability. MLD was obtained from the MIMOC climatology, (Schmidtko et al.,  
338 2013), which was linearly interpolated from its original  $0.5^\circ \times 0.5^\circ$  grid at monthly resolution  
339 to the MODIS grid at daily resolution.

340 Satellite remote sensing of biological activity in surface waters requires ice-free and at  
341 least part of the time cloud-free. The passive sensing methods of MODIS additionally require  
342 a minimum of solar illumination of the scenes (i.e., solar zenith angle  $< 70^\circ$ ; (IOCCG, 2015)).  
343 Consequently, the length of the satellite-observable period used to compute DMSPt means  
344 shortens from all-year-round at latitudes  $< 45^\circ$  to approximately six months (the spring-  
345 summer semester) at  $80^\circ N$ . In addition, the annual DMSPt map in Fig. 3 excludes all land and  
346 ice covered regions. In order to increase data coverage, daily DMSPt composites were binned  
347 to five-day periods and a 46.4 km equal-area sinusoidal grid, (10x10 bins of the original pixel  
348 size). The average distance between a trajectory point and the closest center of a MODIS  
349 pixel is 18 km.

350 Following the same approach as with the ice data average DMSPt from ocean color data,  
351 (OC), along each back trajectory were calculated and will be referred to as OC1 (the last day),  
352 OC2 (the last but one day), and OC5 (days three to five) before arrival at Mt. Zeppelin. In  
353 this procedure missing data were flagged as such, and were not taken into account.

354

355

## 356 2.5 Ice data

357

358 For the interpretation of events of new particle formation observed during the *Oden* cruises  
359 information on pack ice extent under the air masses reaching the sampling points proved



360 crucial (Heintzenberg et al., 2015). Another motivation for utilizing ice data in the present  
361 study is the fact that the Svalbard region experiences large seasonal changes in pack ice cover  
362 which we expect to have strong effects on emissions of particles and their precursor gases.  
363 Thus daily ice concentrations were taken from the NSIDC database (<https://nsidc.org/data>).  
364 The irregularly shaped data gap around the pole caused by the inclination of satellite orbits  
365 and instrument swath was filled with 100% cover. To each hourly position and data of the  
366 back trajectories the ice information in the corresponding maps of ice concentrations were  
367 added and displayed in Fig. 2. On average the closest pixel in the ice maps was about 12 km  
368 off any trajectory point.

369 In the discussion of results we utilize the complement of ice cover, i.e., the amount of open  
370 water because the marine biological processes of interest predominantly take place in the  
371 open water, (Leck and Persson, 1996a). As integral parameters average open water, (OW),  
372 percentages along each back trajectory were calculated and will be referred to as OW1 (the  
373 last day), OW2 (the last but one day), and OW5 (days three to five) before arrival at Mt.  
374 Zeppelin. The most solid ice cover is seen in an area reaching from Northeastern edge of  
375 Greenland via North Pole to Parry Island. A marginal ice zone extends along the east coast of  
376 Greenland to Franz-Josef-Land, and the area between Svalbard and the latter island.

377

378

## 379 **2.6 ERA-Interim data of sea surface temperature**

380

381 Daily Sea Surface Temperature (SST) data for our study period (2006-2015) were  
382 downloaded from the website of the European Centre for Medium-Range Weather Forecasts  
383 (ECMWF). A description of the global atmospheric reanalysis, (ERA-Interim), has been  
384 given by Dee et al. (2011), and a guide to the products and the download procedures can be  
385 found at <http://www.ecmwf.int/en/elibrary/8174-era-interim-archive-version-20>. Briefly,



386 ERA-Interim is an assimilating model reanalysis of the global atmosphere and sea-surface  
387 physical parameters covering the data-rich period since 1979. SST data were downloaded at a  
388 resolution of approximately  $0.56^\circ$  and regrided onto the same 46 km equal-area sinusoidal  
389 grid used for DMSP and cloud fraction, (see below). Ice-covered pixels were screened out  
390 prior to the back-trajectory analysis. In the Arctic region, ERA-Interim has been shown to be  
391 a top performer among a number of atmospheric reanalyses, (Lindsay et al., 2014).

392

393

## 394 **2.7 MODIS cloud fraction**

395

396 Persistent cloud cover limits PPP in Arctic and Sub-arctic seas, (Bélanger et al., 2013), and,  
397 as mentioned above, irradiance at the sea surface, which is largely controlled by cloudiness,  
398 influences  $\text{DMSP}_{\text{dissolved-to-DMS}_{\text{aq}}}$  conversion. Boundary layer clouds are known to be  
399 additional controllers of the surface aerosol (Heintzenberg, 2012). In the summer Arctic low  
400 level clouds and fogs are widespread (Warren and Hahn, 2002). Both scavenging and new  
401 particle formation have been observed in connection with low clouds and fog passages  
402 (Lannefors et al., 1983; Heintzenberg and Leck, 1994; Leck and Bigg, 1999; Heintzenberg et  
403 al., 2006; Karl et al., 2013). Beyond the cloud base derived from the ceilometer we have no  
404 other in situ local or regional cloud information. Thus, we utilize satellite-derived cloud  
405 information.

406 Daily Level-3 global cloud fraction with one-degree resolution was downloaded from  
407 NASA website (<http://modis-atmos.gsfc.nasa.gov>, Hubanks et al., 2015) and extracted for our  
408 region of interest. Briefly, level 3 images correspond to the aggregation of all level 2 images  
409 (1 km resolution) available within the one-degree resolution grid. For a given L2 scene, each  
410 pixel is assigned a value of 1 (cloudy) or zero (clear sky), and then the individual scene values  
411 are averaged over a 24-hour period. Note that a given pixel can be revisited up to six or seven



412 times in the course of a day at high latitudes. Finally, the daily composites were re-projected  
413 to 46.4 km pixels to match the spatial resolution of DMSPt. The average distance between a  
414 trajectory point and the closest MODIS pixel was 18 km.

415 The cloud fraction CF as well as other cloud properties from MODIS have been  
416 extensively used, for instance to study the global spatial and temporal distribution of clouds  
417 over the last decade (e.g., King et al., 2013). Several studies have also successfully  
418 performed validation by comparison with in situ data (e.g., An and Wang, 2015) which  
419 demonstrated the ability of the MODIS-aqua sensor to retrieve cloud cover.

420 Following the same approach as with the ice data and DMSPt, average cloud fractions,  
421 (CF, see Table 1), along each back trajectory were calculated and will be referred to as CF1  
422 (the last day), CF2 (the last but one day), and CF5 (days three to five) before arrival at Mt.  
423 Zeppelin. Missing data are flagged as was done with DMSPt data.

424

425

### 426 **3. Three approaches to identifying events of new particle formation**

427

428 There are no definitive and no generally accepted methods to identify or predict NPF-events  
429 in atmospheric time series of aerosol data. Thus, in the present study we explored different  
430 approaches with varying degrees of complexity to identify such events. We emphasize that  
431 none of these approaches explicitly is connected to diel cycles such as in Dal Maso et al.,  
432 (2005) or makes any assumptions about the time of day during which new particle formation  
433 occurs. Three objective search algorithms were written in FORTRAN to analyze the time  
434 series of hourly records of aerosol parameters in search of new particle formation:

435 1. The simplest approach of upper percentiles (PCT-approach), assumes that NPF-events are  
436 characterized by extremely high concentrations of small particles in terms of N25 (see  
437 Table 1). The key parameter characterizing each PCT-event was the value of N25



438 averaged over a fixed number of hours, ( $N_{25_{av}}$ ), after the nominal start of an event, (see  
439 below). With  $N_{25_{av}}$  also a nominal length of PCT-events was defined as the number of  
440 hours after the start of an event by which  $N_{25}$  sank to less than half of  $N_{25_{av}}$ .

441 2. The more specific approach of diameter growth (DGR-approach) builds on the temporal  
442 development of the particle size distribution in terms of a systematic growth of the  
443 diameter  $D_{50}$  (see section 4.1) to find the classical “Banana Type” of NPF-event,  
444 (Kulmala et al., 2004). The key parameter characterizing each DGR-event was the average  
445 growth of  $D_{50}$  during the nominal event length  $NUC$ , (see below). For this approach the  
446 nominal length of events was reached when the running two-hour average growth fell  
447 below the value one.

448 2. The most complex approach of multiple-size events, (MEV-approach), searches for events  
449 with concurrent appearance of concentration increases in several size classes below 60 nm  
450 diameter (Karl et al., 2013; Leck and Bigg, 2010). The key parameter characterizing each  
451 MEV-event was the relative concentration increase averaged over the chosen size classes  
452 below 60 nm during the nominal event length  $NUC$ , (see below). As with PCT-events a  
453 nominal length of MEV-events was defined as the number of hours after the start of an  
454 event by which  $N_{25}$  sank to less than half of  $N_{25_{av}}$ .

455

456 Three time-related parameters were commonly defined for all three approaches:

- 457 1. Nominal NPF-event length, ( $NUC$ ) was nine hours.
- 458 2. Pre-event periods, ( $PRENUC$ ), from which increases in diameters or number  
459 concentrations were calculated, were six hours.
- 460 3. Reference periods, ( $REF$ ), before  $PRENUC$  and after  $NUC$  periods were defined in order  
461 to compare event and pre-event data with non-event conditions. Each of these reference  
462 periods had the length of half the sum of pre-event plus event time periods, making the  
463 total reference time period of each event as long as that of the event itself.



464 Besides these common characteristic lengths individual fixed thresholds were chosen and  
465 discussed below for each approach in order to generate at least 200 unique events per  
466 approach, (see Table 2).

467 The aerosol data used to define the NPF-events were complemented by a large number of  
468 environmental parameters. The primary temporal resolution of the environmental parameters  
469 was between one minute (C25, cf. Table 1) and five days (DMSPt, cf. Table 1). C25 was  
470 calculated as 25% percentile on an hourly basis. The parameters with resolutions higher than  
471 an hour (OW, CF, and OC, cf. Table 1) were evaluated along the hourly back trajectories.  
472 While this procedure yielded hourly varying results even of OW, CF, and OC it has to be kept  
473 in mind that this hourly variability is the result of hourly resolved trajectories traversing the  
474 grid; the low primary temporal resolutions of the OW, CF, OC, and chemical parameters  
475 remain. For these slowly varying parameters the REF periods before and after the events  
476 were extended to one day beyond the longest primary resolution, i.e., six days.

477 For two reasons the three search algorithms may yield temporarily redundant results, i.e.,  
478 they may identify the same events. One, they go independently through the same time series  
479 of aerosol data, possibly causing inter-approach redundancy. Two, each algorithm goes  
480 through the time series hour by hour, thus allowing for temporal overlap of events found by  
481 each approach, (intra-approach redundancy).

482 The three types of events were assumed to be mutually exclusive and potentially being  
483 caused by different sets of conditions for new particle formation. Thus, a FORTRAN  
484 procedure was developed to eliminate both intra and inter-approach redundancy while  
485 maintaining a maximum of identified NPF-events. To remove intra-approach redundancy the  
486 procedure identifies overlapping events within each approach. Of each ensemble of such  
487 overlapping events the one with the strongest key parameter of the respective approach  
488 (growth of D50, or concentration increases as defined above) is retained. Next, inter-  
489 approach redundancy is addressed by the procedure. However, there is no unique solution to



490 the problem of the partly redundant three time series of events. In order to avoid any  
491 preference of one or several types of events in the tests of inter-approach overlap pairs of  
492 events of different approaches are chosen at random and compared for overlap. This random  
493 comparison is done as often as the product of the number of events of the three approaches.  
494 This rather time-consuming random test yields stable numbers of non-overlapping events  
495 within less than one percent, irrespective of the order in which the events of the three  
496 approaches were arranged for the test. By removing intra and inter-approach redundancy in  
497 the first two steps of the procedure a number of time periods will be “freed”. Consequently,  
498 in a last step, the procedure tries to fill the “freed time periods” non-redundantly with events  
499 of the three approaches that had been eliminated in the first two steps. Table 2 collects total  
500 numbers and unique numbers of events for each approach. In the rest of the paper only non-  
501 redundant events will be discussed. The total number of new particle formation events will  
502 be shortened to TNPF.

503

504

### 505 **3.1 The upper percentile of N25 (PCT-approach)**

506

507 Events of new particle formation were identified by time periods in which N25 was  
508 consistently, i.e. on average for three hours, above a set threshold. With a threshold of the  
509 93%-percentile ( $170 \text{ cm}^{-3}$ ) 4143 PCT-events were identified in the total data set, only 240 of  
510 which were unique because most of them overlapped with event or pre-event times of the  
511 other two approaches. Average N25 during these unique events was  $330 \text{ cm}^{-3}$  and the average  
512 length of events  $4 \pm 0.9 \text{ h}$ , (one standard deviation).

513 Fig. 4, (top), shows the average temporal development of the relative size distributions for  
514 the unique PCT-events as in the results in Karl et al. (2013), i.e. relative concentrations were  
515 formed by dividing the absolute number concentrations by the average total number during



516 the six-hour pre-event time periods. The events are characterized by a nearly monomodal  
517 distribution around 20 nm that broadens somewhat around the nominal start of the events.  
518 During the last three hours before the events D50 decreased slightly and returned to the pre-  
519 event level during the nine NUC hours.

520 In connection with PCT-events average aerosol parameters NTO through N300 showed an  
521 average increase by a factor of 2.2 during PRENUC-periods, which was maintained on an  
522 average level of 1.5 during the events. The aerosol-chemical parameters  $\text{Na}^+$ ,  $\text{nssSO}_4^{-2}$ , and  
523 MSA were on an average level of 20% of their reference value. The average environmental  
524 parameters indicate a strong increase by a factor of 14 in solar radiation and a lifting of cloud  
525 base before the events. During the events the level of solar radiation was still elevated by a  
526 factor of six above its reference value. As a consequence temperature at the station was up by  
527 2 – 3 degrees. Precipitation 12 h before trajectory arrival time, (SP12) was a factor of five  
528 above reference levels for air arriving during NUC-periods, whereas SP35 to SP5D were  
529 below their respective reference levels. Cloud fractions were slightly raised 12 - 48 h before  
530 air arrival. Of the ocean parameters more open water was met by trajectories 12 to 24 before  
531 their arrival with ocean temperatures 12 to 48 h before trajectory arrival having been up to  
532 four degrees warmer than their respective reference values. On average DMSPt-parameters  
533 OC24 through OC5D showed were raised by a factor of two above their reference value.

534 In Fig. 5, (left top panel), average trajectory height profiles during PRENUC and NUC-  
535 periods are displayed. Widely varying vertical air mass paths occurred before and during  
536 PCT-events. Median vertical trajectory paths during PRENUC and NUC times indicated air  
537 coming from some 300 m above station level five days ago sinking to about one hundred  
538 meters above station level during the last two days before arrival. The upper quartiles of the  
539 PCT-height profiles point at strong subsidence before air mass arrival.

540 The right top panel in Fig. 5 maps average horizontal trajectory positions in 12 h steps in  
541 months having at least ten PCT-events, i.e., May - September. Filled circles around the



542 trajectory positions comprise 95% of all events. The monthly average horizontal trajectory  
543 direction during PCT-events mostly was from the northwest. In June and July the trajectories  
544 reached farthest into the multiyear ice cover northeast of Greenland. Only during September  
545 the back trajectories covered ice-free and marginal ice areas in the Fram Strait. We note that  
546 the five-day back trajectories of PCT-events, (and of the other two approaches as well), stayed  
547 within some 800 km of Mt. Zeppelin.

548

549

### 550 **3.2 The diameter growth (DGR) approach**

551

552 The DGR-approach to identify events of new particle formation builds on the classical  
553 concept of particle growth through condensable vapors after an initial nucleation of sub-five  
554 nanometer particles that cannot be observed with the available instrumentation, so called  
555 “Banana-type” (Kulmala et al., 2004). The respective algorithm utilizes the parameter D50,  
556 (see Table 1), and requires a growth of this diameter by at least a factor of 1.5 after the  
557 nominal start of an event. With this threshold the algorithm searched through all 87646 hours  
558 of the ten-year record and found 1199 DGR-events of new particle formation. After  
559 eliminating cases of temporal overlap with the other two approaches 235 unique events of this  
560 type remained, (see Table 2). Other or more DGR-events could have been found by  
561 shortening the nominal nine NUC hours. For two reasons we refrained from discussing  
562 shorter growth periods in the DGR-approach. Maintaining common-length NUC periods  
563 facilitated the comparison of results of the three approaches. Furthermore, reducing the  
564 growth period would also make PCT and DGR-events ever more similar.

565 Starting with an average value of  $D50 \approx 16$  nm at the nominal start of DGR-events an  
566 average growth rate of  $1.8 \text{ nmh}^{-1}$  is derived, which is in the range of  $1 - 2 \text{ nmh}^{-1}$  derived by  
567 Ström et al. (2009) for new particle formation in the lower boundary over Ny-Ålesund,



568 Spitsbergen but considerably lower than the maximum growth rate of  $3.6 \text{ nmh}^{-1}$  reported by  
569 Asmi et al. (2016) for July at the Siberian station Tiksi at the coast of the Laptev Sea. The  
570 average length of DGR-events was  $10 \pm 1 \text{ h}$ , (one standard deviation).

571 The average temporal development of the relative number size distribution during DGR-  
572 events is presented in Fig. 4, (center). After a decrease of the sub-50 nm diameter median  
573 from about 25 to 16 nm during the six hours before the nominal start of the events D50  
574 increases systematically during the following nine NUC hours with somewhat reduced growth  
575 towards the end of the event.

576 During the PRENUC-periods particle number concentrations N300, and the condensation  
577 sink, (CS), decreased relative to the reference periods before and after the events.  
578 Subsequently, during the NUC periods the strongest increases was found for N60.  
579 Environmental parameters around air mass arrival showed a strong lifting of cloud base,  
580 (C25), and an extremely high increase in solar radiation, (by a factor of 11 during PRENUC  
581 and by a factor of 60 during NUC periods). However, 12 h before air arrival precipitation had  
582 been up by a factor of 2.5. Cloud fractions were down to about 70% of their reference values  
583 24 through 48 h before air arrival. Of the chemical aerosol parameters  $\text{Na}^+$  and  $\text{nssSO}_4^{-2}$   
584 showed an increase of 2.6 and 2.3, respectively. OC12 and OC48 were slightly higher than  
585 reference level before and during the events. Sea surface temperatures T24 were raised by  
586 nearly one degree whereas earlier SST-values, (T36 – T5D), were up to one degree below  
587 reference values.

588 Fig. 5, (left center panel), shows statistics of the vertical air movement before trajectory  
589 arrival during DGR-events at Mt. Zeppelin covering a wide range of vertical movements  
590 between 200 m and beyond 1500 m height. During the days when elevated DMSPt levels  
591 were noted median trajectory heights were six to nine hundred meters. Median trajectories  
592 during PRENUC times dipped down to the station level, (474 m a.s.l), about one day before



593 arrival, albeit lifted and subsided again shortly before arrival. Vertical trajectory pathways  
594 will be discussed further in Section 4.2.

595 Monthly average trajectory positions and their variability in connection with DGR-events  
596 are shown in Fig. 5, (center right panel). The months April through October had at least ten  
597 DGR-events per month. As with PCT-events the general trajectory direction was from the  
598 northwest, mostly staying for several days over the marginal ice zone between northeastern  
599 Greenland and eastern Svalbard. During the earliest month of April with 14 DGR-events the  
600 back trajectories reached farthest south into the ice-free parts of the Fram Strait.

601

602

### 603 3.3 The Multiple-size approach (MEV)

604

605 Leck and Bigg (2010) and Karl et al. (2013; 2012) discussed a type of new particle formation  
606 that to date only has been reported from the summer Arctic. During these MEV-events high  
607 ultrafine particle concentrations appear concurrently in a broad diameter range reaching from  
608 under 10 to some 60 nm. We simulated this type in a search that required the concurrent  
609 increase of NTO, N20, N40, and N60, (cf. Table 1), as averaged over the first three NUC  
610 hours by a factor  $\geq 1.6$  over their respective averages during the six (PRENUC) hours. Over  
611 the ten years of data 1191 such events of this type were identified, 266 of which remained  
612 after removal of those overlapping with events of other approaches. During these unique  
613 events the average concurrent concentration increase was 4.7 and the average length of the  
614 events  $12 \pm 0.8$  h.

615 The bottom part of Fig. 4 shows the average temporal development of relative number size  
616 distributions before and during MEV-events. The development before the nominal start of  
617 MEV-events is more complex than during the PRENUC-periods of the first two types of  
618 events. Intermittently a mode around seven nanometers shows up that broadens and becomes



619 more prominent about two hours before the nominal start of events. The major PRENUC-  
620 mode around 25 nm also broadens and becomes more prominent towards NUC. A weak  
621 mode exists during PRENUC around 120 nm and hardly any particles beyond 400 nm. D50  
622 sinks from 25 to about 20 nm and stays below 25 nm through the MEV-events even though  
623 number concentrations increase during the first NUC-hours by more than a factor of five.

624 During NUC-periods all particle number concentrations increased, on average by a factor  
625 of 1.6. Average solar radiation also increased by about 90% above reference level during  
626 NUC-periods. Of the chemical parameters  $\text{nssSO}_4^{-2}$  showed an increase by a factor of three  
627 during PRENUC and NUC-periods, and MSA a slight increase during PRENUC-periods. On  
628 one hand, precipitation 12 h, and 36 to 48 h before trajectory arrival, (SP12, SP48), were  
629 above reference levels for air arriving during PRENUC-periods. On the other hand, during  
630 PRE, SP24, SP36, an SP5D indicated dry conditions during PRENUC and NUC-periods.  
631 Only three to five days before air arrival slightly increased cloud fractions were noted. Sea  
632 surface temperatures up to five days before trajectory arrival were on average about one  
633 degree lower than their reference values. DMSPt parameters OC12 to OC36 were raised by  
634 factors of 1.3 and 1.6 during PRENUC and NUC-periods, respectively.

635 Percentiles of vertical trajectory coordinates prior to and during MEV-events are displayed  
636 in Fig. 5, (bottom left panel). During the events, and even stronger during the PRENUC  
637 periods median trajectories had been below 500 m for more than four days. Furthermore, the  
638 final air approach to Mt. Zeppelin mostly came from below the station level. Upper quartiles  
639 of the vertical trajectory positions are substantially lower than with DGR-events. We note,  
640 however, that a short excursion above station level occurred in the upper quartiles during the  
641 last three hours before arrival.

642 The bottom right panel of Fig. 5 gives the monthly average trajectory positions and their  
643 variability in connection with MEV-events. The months April through October had at least  
644 ten MEV-events per month. As with the other approaches the general trajectory direction was



645 from the northwest, albeit with stronger swings towards the ice-free areas south of Svalbard  
646 early and late in the season, (April, May, and September). Interestingly, the trajectories of the  
647 11 MEV-events in October were directed nearly straight north from the North Pole.

648 Summarizing differences and commonalities among the results of the three approaches we  
649 can state that the length of the events increases from four to ten and twelve, going from PCT  
650 to MEV-events. PCT-events are characterized by lower-than-reference aerosol-chemical  
651 parameters.  $\text{Na}^+$  and  $\text{nssSO}_4^{-2}$  show strong increases in the other two types of events:  $\text{Na}^+$  in  
652 connection with DGR-events and  $\text{nssSO}_4^{-2}$  in connection with MEV-events. Both, PCT and  
653 DGR-events exhibit strong increases in solar radiation. Precipitation before air arrival was  
654 raised at varying times in connection with the three types of events. Cloudiness bot increased  
655 and decreased at varying times before air arrival with the three types of events. Increased  
656 open water under the trajectories was strongest with DGR-events and least important with  
657 MEV events. Only in connection with PCT-events strongly raised sea surface temperature  
658 were noted before trajectory arrival. DMSpt related ocean parameters were raised to varying  
659 degrees and at varying times before all NPF-events, most strongly in connection with PCT-  
660 events and least in connection with DGR-events.

661

662

#### 663 **4. Discussion**

664

##### 665 **4.1. Environmental setting**

666

667 The discussion of the results on new particle formation in the Svalbard region builds on the  
668 variability of new particle formation and related environmental parameters on scales of  
669 months, and days. Fig. 1 gives an overview over the geographic areas which were covered by  
670 one, two, and five-day back trajectories to Mt. Zeppelin during the ten years of the present



671 study covering the months March through October. This figure illustrates that air arriving at  
672 Mt. Zeppelin during the ten summers of the present study came from widely varying regions  
673 from the central ice-covered Arctic via the northern seas and northernmost Scandinavia to  
674 Greenland. One-day back trajectories cover a roundish area from the central east coast of  
675 Greenland via northern Scandinavia to Franz-Josef-Land, North Pole and back to the north  
676 coast of Greenland. Excluding inner Greenland this area is widened by roughly 500 km by 2-  
677 day back trajectories and by at least another 500 km by 5-day back trajectories reaching over  
678 most of Greenland and the adjacent seas west of Greenland. This is a much wider region  
679 from which air may reach Mt. Zeppelin as compared to sites in the inner Arctic as illustrated  
680 in Fig. 2 of Heintzenberg et al. (2015).

681 On the path of trajectories to Mt. Zeppelin quite different ice conditions were met (see,  
682 Fig. 2). On average North Atlantic open waters reached around West Spitsbergen all the way  
683 to Nordaustlandet. Drift ice was passed over by trajectories along the whole east coast of  
684 Greenland. One-day trajectories passed over the marginal ice zone from the Fram Strait to  
685 Franz-Josef Land but also over more contiguous ice close to the North Pole. At times, with  
686 five-day back trajectories, even the marginal ice regions of Baffin Bay and Beaufort Sea were  
687 reached.

688 The long-term geographical distribution of DMSPt in Fig. 3 reflects the water conditions  
689 for phytoplankton biomass around Svalbard. Directly at the coasts of Greenland and Eurasia  
690 increased nutrient availability in coastal and shelf waters (due to continental run-off and  
691 enhanced hydrodynamics) cause localized areas of high DMSPt values. The low DMSPt  
692 values further out along the coast of Greenland are due to sea ice reaching through the Fram  
693 Strait far south, (see Fig. 2). A prominent feature in the regional DMSPt distribution is the  
694 tongue of high DMSPt, (intense blue color), and thus high phytoplankton biomass east of this  
695 area, reaching from Spitsbergen to roughly Jan Mayen that lies within one-day back  
696 trajectories. Northward-flowing Atlantic waters, carried by the West Spitsbergen Current,



697 and southward-flowing fresh surface waters from melting ice, and recirculated Atlantic  
698 waters, carried by the East Greenland Current (Rudels et al., 2005) are meeting. The layering  
699 created by water masses of different density stabilizes the water column and traps  
700 phytoplankton cells at well-lit depths. If sufficient nutrients are available, this can lead to the  
701 development of large phytoplankton blooms, which can result in high concentrations of  
702  $\text{DMS}_{\text{aq}}$ , (see Fig. 2 in Leck and Persson, 1996a).

703 In the ten-year average cloud fractions systematic differences in cloudiness appear.  
704 Depending on transport pathways as identified by the back trajectories, cloudiness varies on  
705 the way to Spitsbergen. The ice-covered areas, (cf. Fig. 2), from the east coast of Greenland  
706 to Franz-Josef-Land exhibit somewhat lower cloud fractions than the ice-free regions  
707 southwest to east of Spitsbergen.

708

709

#### 710 **4.2 Seasonal variability**

711

712 Seasonal changes are discussed in terms of monthly averages taken over the ten-year study  
713 period. As expected in Earth's polar regions the seasonal variability of all environmental  
714 parameters is very high as exemplified by the solar flux, (SFL), and the air temperature,  
715 (TEM), at Mt. Zeppelin in Fig. 6. Due to the seasonal change in cloudiness, (cf. Fig. 7), the  
716 seasonal distribution of SFL is not quite symmetrical about midsummer but is skewed slightly  
717 towards the cloud minimum in spring. The air temperature, however, does not peak before  
718 July and has a broad shoulder into fall and winter. The first, and partly absolute maxima, of  
719 the seasonal distributions of NPF-events in Fig. 6 coincide with that of the SFL but then drop  
720 of more slowly towards fall than solar radiation. In particular, MEV-events do so and even  
721 have their main maximum in August. The occurrence of all NPF-events drops off sharply in  
722 October. Whereas May as the first month with larger numbers of events is dominated by



723 PCT-events, followed by DGR and then MEV-events, the contributions of the three NPF-  
724 types are reversed in the last month with high NPF-numbers, i.e., September.

725 Fig. 6 clearly shows that the formation of new particles in the Svalbard region is not  
726 controlled by the late winter-to-early-spring phenomenon of Arctic haze peaking with highest  
727 sulfate-concentrations in March, (cf. Fig. 3 in Heintzenberg, 1989, and Fig. 6), which has a  
728 minimum in the total number of NPF-events. This minimum is in contrast with the maximum  
729 in new particle formation rates found by Croft et al. (2016a) with their global aerosol model.  
730 The high numbers of accumulation mode particles during the Arctic haze months in late  
731 winter and spring yield the annual maximum in condensation sink, (CS in Fig. 6), which  
732 could quench nucleation events and subsequent growth. Thus, even though photochemistry  
733 may produce significant amounts of nucleating material, the freshly formed particles will not  
734 grow to stable size before they are removed via either deposition or coagulation as discussed  
735 by Tunved et al. (2013) and others. An alternative explanation of the late onset of NPF-  
736 events in TNPF in spring lies in the marine biological processes not being activated nearby  
737 during the Arctic haze period yet, (Heintzenberg and Leck, 1994).

738 Fig. 7 collects the seasonal variation of environmental parameters as averaged along the  
739 back trajectories to Mt. Zeppelin. From their minimum in March-April open water conditions  
740 improve until September, after which the pack ice extent under the trajectories rapidly  
741 increases again. The widening open water areas are reflected in sea surface temperatures  
742 under the trajectories that increase until September before they drop off strongly in October.  
743 Consequently, because of its connection to marine biological activity DMSPt increases in the  
744 euphotic zone from first photosynthetic light in May until it evens out around July and drops  
745 off in October. Largest DMSPt values are reached in the vicinity of Svalbard, (cf. OC12 in  
746 July and August in Fig. 7), i.e. considerably later than MSA. The ending of DMSPt-curves in  
747 October is due to the lack of data not due to zero-DMSPt. Still, DMSPt concentrations are  
748 expected to be low at this time of the year at temperate to polar latitudes due to low



749 phytoplankton biomass and low light exposure, (see Fig. 9 in Galí et al., 2015). In terms of  
750 the MODIS-derived cloud fraction cloudiness increases rapidly from its minimum in April  
751 and evens out on a plateau of 80–90% after July. The spring-minimum in cloudiness is  
752 confirmed by the maximum in cloud base as indicated by C25 in Fig. 7. This seasonal  
753 distribution of cloudiness does not correspond to the classical picture of near-surface  
754 cloudiness that exhibits near cloud-free conditions in winter and mostly overcast with Arctic  
755 stratus and fogs during the summer months (Warren and Hahn, 2002; Huschke, 1969). We  
756 explain the difference by the specific atmospheric pathways covered by the back trajectories  
757 of the present study (cf. Fig. 1). Trajectory-averaged precipitation parameters (SP12-5D in  
758 Fig. 7) have minima in the period April–May, from which they increase towards their  
759 maxima in fall and winter.

760 The chemical aerosol information derived from the analyses of filters samples has a  
761 relatively low temporal resolution of at least one day combined with frequent gaps of several  
762 days in between samples. Thus, it cannot directly be related to the time periods of NPF-  
763 events. The seasonal distribution of chemical tracers, however, yields important information  
764 about new particle formation. Taken over the whole year  $\text{nssSO}_4^{2-}$  in Fig. 6 is largely  
765 anthropogenic, (Heintzenberg and Leck, 1994), and has its maximum during the peak of  
766 Arctic haze in March and April and its minimum in August, which does not match any  
767 seasonal distribution of NPF-events. We also plotted  $\text{Na}^+$  in Fig. 6 as a tracer of the inorganic  
768 marine aerosol components sea salt.  $\text{Na}^+$  decreases from its winter maximum to its summer  
769 minimum in June/July, again without similarity to the NPF-distributions. Instead, the  
770 seasonal distribution of  $\text{Na}^+$  rather closely follows that of the trajectory-derived wind speed  
771 during the last hour before arrival, (not shown in the figure). Wind speed as driver for sea salt  
772 production is a well established phenomenon (Blanchard and Woodcock, 1957). After a steep  
773 rise in April MSA in Fig. 6 sharply peaks in May and then gradually drops off towards its  
774 minimum in October, more gradually than reported for data taken from 1991 to 2004 by



775 Sharma et al. (2012) and earlier than reported by Heintzenberg and Leck (1994), both at the  
776 same station. Our seasonal distribution of MSA most closely resembles that of SFL, in Fig. 6,  
777 albeit with its peak in May a month earlier than SFL and more strongly skewed towards  
778 spring. According to Leck and Persson (1996b) on average the concentrations of the marine  
779 biogenic sulfur components, (DMS and MSA), fell with a decline rate of about 30% per week  
780 approaching zero values in September explained by reduced ppp (Leck and Persson, (1996a),  
781 (consistent with Becagli et al., 2016).

782 As MSA is the only measured aerosol component with exclusively marine biogenic  
783 sources, we illustrate its seasonal distribution in greater detail in Fig. 8. In this figure MSA-  
784 concentrations measured on Mt. Zeppelin have been extrapolated along 5-day back  
785 trajectories, forming monthly average monthly maps of potential MSA-sources during the  
786 biologically most active months of March through October.

787 Fig. 8 yields several items of information that are relevant to the issue of new particle  
788 formation. Early in spring the biological aerosol sources are limited to the North Atlantic and  
789 Norwegian Sea. In April the tongue of newly opened waters between Novaya Zemlya and  
790 Franz-Josef-Land seemingly is beginning to become biologically active. In May this area  
791 widens towards the Barents Sea while the North Atlantic also becomes more active, reaching  
792 the Fram Strait. In August two wide potential source regions cover the region from Northern  
793 Greenland to the northern end of Scandinavia and the region Barents to Kara Sea. In  
794 September even the pack ice north of Svalbard becomes biologically active, (Leck and  
795 Persson, 1996a), and shows potential MSA sources, in particular, north of the northern coast  
796 of Greenland. Finally, the very weak potential MSA sources in October appear to be situated  
797 mainly over the Kara Sea and over the North Atlantic.

798 How do these seasonal distributions compare to those of the NPF-events identified by the  
799 three search-approaches defined in Section 3? To address this question we constrained the  
800 average seasonal distribution of environmental parameters to those hours that had been



801 identified by the NPF-events of the three approaches. However, none of the individual  
802 seasonal distributions of constrained environmental parameters follows closely any of the  
803 NPF-events. In particular, the main MSA peak remains in May, thus one month earlier than  
804 any peak of the NPF-occurrences. To elucidate further potential differences in the three types  
805 of NPF-events we return to the discussion of vertical pathways of related back trajectories,  
806 (see Fig. 5). In this figure all three types of NPF-events exhibit a wide range of vertical  
807 trajectory paths. As we expect the regional sources of primary particles and particle  
808 precursors to be at or near the surface we segregated the NPF-events into subpopulations with  
809 back trajectories that remained a given time below 500 m, (roughly station level). In Fig. 9  
810 we collected the results concerning the 93 NPF-events that occurred with trajectories under  
811 the 500 m limit, i.e., roughly 12% of all events. The top panel shows that the related  
812 trajectories not only stayed below 500 m through most of the last five days before arrival but  
813 close to the surface until they started rising to the station level about 24 h before arrival. The  
814 peak of the sum of event occurrences now coincided with the main MSA peak in May, (see  
815 center panel in Fig. 9). For DGR-events the May-maximum was particularly strong whereas  
816 the PCT-predominantly occurred in May and June and MEV-events remained clustered  
817 around the later part of summer, possibly coupled to SST and DMSPt.

818 A number of environmental parameters indicated substantial deviations from their  
819 respective reference values during the months with most frequent occurrence of this sub-  
820 population of NPF-events. Strongest deviations were noted for precipitation that was elevated  
821 above reference levels two to five days before trajectory arrival, most prominently for DGR-  
822 events in May, (by a factor of six 36 h before trajectory arrival). Strong positive deviations in  
823 aerosol-chemical parameters only occurred with  $\text{Na}^+$  in PCT and MEV-events, indicating  
824 relatively high wind speeds near sea surface in the related air masses. MSA was elevated up  
825 to 50% above reference levels only during MEV events. Elevated levels of DMSPt were



826 noted with all three types of NPF-formation, most prominently for DGR-events 12 to 36  
827 hours before which DMSPt was raised by factors up to 1.7 relative to reference levels.

828 The bottom panel of Fig. 9 gives average trajectory positions in 12 h steps for the months  
829 May through September. The circles around the steps comprise 95% of all trajectories.  
830 During all months the trajectories stayed in the ice-free and marginal ice zone between Fram  
831 Strait and Eastern Svalbard as illustrated by average July ice cover for the ten study years,  
832 (for average monthly ice covers cf. Fig. 8). In particular during the earliest and latest months  
833 of May and September the trajectories swing farthest south over the open water south of  
834 Svalbard. We note that the complementary sub-population of results with trajectories  
835 remaining above station level did not yield results that differed strongly from those for the  
836 whole population of back trajectories.

837 As a last step in the discussion of seasonal variations in new particle formation a model is  
838 formulated that describes the average sum of NPF-events, (TNPF), as a function of three  
839 parameters, two of which are directly measurable at the site. With the linear combination of  
840 the solar flux, (SFL,  $\text{Wm}^{-2}$ ), average sea surface temperature under back trajectories 36 to 48  
841 hours before their arrival at the site, (T48, °C), and condensation sink, (CS,  $10^5 \text{ s}^{-1}$ ):

842

$$843 \quad TNPF = 0.57 \cdot SFL + 15.4 \cdot T48 - 0.69 \cdot CS$$

844

845 TNPF as shown in Fig. 10, can be described within an average deviation of 5% taken over the  
846 major months with new particle formation, April - October. Any other of the sea surface  
847 parameters describes TNPF less well.

848

849

850

851



### 852 4.3 Diurnal variability

853

854 Average hourly occurrence of the three types of NPF-events is plotted in Fig. 11, (top). The  
855 three approaches yield rather similar diel variations. From their minimum during the night  
856 and early morning hours they reach their maximum occurrence between 12 and 16 h UTC in  
857 the afternoon. One might expect the differences between the NPF-types to be due to the  
858 requirement of the three types of NPF formation being mutually exclusive. However, this  
859 constraint does not exclude that they occur at the same time of day, only that they occur at the  
860 same time on the same day.

861 Over the continents new particle formation and growth events of the classical “Banana-  
862 type” usually exhibit an increase in measurable precursors such as sulfuric acid shortly after  
863 sunrise followed by the detection of increased numbers of nanometer-sized particles between  
864 one and two hours later (Kulmala et al., 2004), who deduce a connection to photochemically  
865 produced condensable vapors from this daily pattern. In the Svalbard region the sun is up all  
866 day between mid-April and the end of August. Consequently we would expect the  
867 photochemical production of condensable vapors to have a smaller diurnal amplitude than at  
868 lower latitudes, which in turn should even out the diurnal pattern of NPF-events to some  
869 degree. Despite the relatively small daily variations in solar elevations the solar flux on Mt.  
870 Zeppelin varied on average by more than a factor of five during the sunlit days (see curve  
871 SFL in Fig. 11, bottom). The daily maximum of SFL between 12 and 15 UTC coincides well  
872 with the average diel change in N25 and NPF-occurrence. As expected in particle growth due  
873 to condensable vapors after initial nucleation the daily maximum in N10 precedes that of N25  
874 by a few hours.

875 The other process controlling the development of newly formed small particles is the  
876 diurnal development of the planetary boundary layer, (Kulmala et al., 2004). We have no  
877 data on the daily variation in boundary layer structure over or near the measurement site. The



878 ceilometer data yield the only high-resolution information with some connection to the  
879 structure of the planetary boundary layer. During the summer months these data show a  
880 consistent daily variation with a jump in most frequent hourly cloud base by about 100 m  
881 from about 1570 m after 09 UTC with rather stable values following until 16 UTC, after  
882 which cloud base decreases again to values comparable to the early morning hours. The  
883 hourly medians of the vertical displacement parameter DZ, (see Fig. 11, bottom), provide a  
884 clearer diurnal variation. While being negative throughout the day, i.e. indicating subsiding  
885 air during the last hour before arrival at Mt. Zeppelin, DZ indicates the weakest subsidence in  
886 early afternoon. We interpret diurnal variation in cloud base and DZ as indicative of local  
887 clearing and convection during the day that may be conducive to photochemical processes  
888 and mixing in the boundary layer, both of which would be enhancing new particle formation.

889

890

## 891 5. Conclusions

892

893 Three different types of events of new particle formation, (NPF), were identified through  
894 objective search algorithms formulated for the present study. The first and simplest algorithm  
895 utilizes short-term increases in particle concentrations below 25 nm, (PCT-events). The  
896 second one builds on the growth of the sub-50 nm diameter-median, (DGR-events), and is  
897 most closely related to the classical “banana-type” of events, (Kulmala et al., 2004) involving  
898 the presence of photochemically generated DMS oxidation precursors. The third and most  
899 complex, so-called multiple-size approach to identifying NPF-events builds on the hypothesis  
900 of Leck and Bigg (2010), suggesting the concurrent production of polymer gel particles at  
901 several sizes below about 60 nm, (MEV-events).

902 With these algorithms NPF-events were identified in a ten-year record of hourly number-  
903 size distributions taken at the research station on Mt. Zeppelin, Spitsbergen. As a first and



904 general conclusion we can state that NPF-events are a summer phenomenon and not related to  
905 Arctic haze, which is a late winter-to-early spring event. The seasonal distribution of the  
906 available information on cloudiness does not suggest any direct connection with NPF-  
907 formation. The MODIS derived cloud fraction generally is very high (70 – 90%) and rather  
908 evenly distributed over the Svalbard region during the months with high frequencies of NPF-  
909 events. As already reported in Tunved et al. (2013) NPF-events appear to be somewhat  
910 sensitive to the available data on precipitation derived from the trajectory model, in particular  
911 when constrained to cases with back trajectories staying below 500 m. In this subpopulation  
912 of NPF-events DGR-events show the strongest change in precipitation parameters in  
913 connection with new particle formation.

914 The seasonal distribution of solar flux suggests some photochemical control that may  
915 affect marine biological processes generating particle precursors and/or atmospheric  
916 photochemical processes that generate condensable vapors from precursor gases. Whereas  
917 the seasonal distribution of the biogenic MSA follows that of the solar flux it peaks before the  
918 maxima in NPF-occurrence. For PCT-events, and more distinctly so for DGR-events, this  
919 one-month delay disappears in the subpopulation with back trajectories staying below 500 m.  
920 MEV-events, however, maintain their peak occurrence later in summer and early fall.

921 With the limited information on particle size, composition, particle precursors, and  
922 environmental conditions no definitive statements can be made about the processes leading to  
923 the formation of new particles in the Svalbard region. A host of findings, however, point to  
924 varying and rather complex marine biological source processes. The potential source regions  
925 for all types of new particle formation appear to be restricted to the marginal ice and open  
926 water areas between Northeastern Greenland and Eastern Svalbard. During earliest and latest  
927 months with high numbers of NPF-events the back trajectories reach farther south into the  
928 open waters of the North Atlantic. Depending on conditions yet to be clarified new particle  
929 formation may become visible as short bursts of particles around 20 nm, (PCT-events), longer



930 events involving condensation growth, (DGR-events), or extended events with elevated  
931 concentrations of particles at several sizes below 100 nm, (MEV-events). The seasonal  
932 distribution of NPF-events peaks later than that of MSA and, DGR and in particular of MEV-  
933 events reach into late summer and early fall with much open, warm, and DMSPt-rich waters  
934 around Svalbard, promoting the production of *Phaeocystis pouchetii* together with polymer  
935 gels. Consequently, a simple model to describe the seasonal distribution of the total number  
936 of NPF-events can be based on solar flux, and sea surface temperature, representing  
937 environmental conditions for marine biological activity, and condensation sink, controlling  
938 the balance between new particle nucleation and their condensational growth. Based on the  
939 sparse knowledge about the seasonal cycle of gel-forming marine microorganisms and their  
940 controlling factors we hypothesize that the seasonal distribution of DGR and more so MEV-  
941 events reflect the seasonal cycle of the gel-forming phytoplankton.

942 Despite the rather small diel changes expected during the summer Arctic there is a  
943 significant diurnal variation in aerosol and environmental parameters. Diurnal distributions  
944 of particle numbers below ten, (N10), and below 25 nm, (N25) follow that of the solar flux  
945 rather closely with a maximum between 14 and 16 UTC with the maximum of N10 occurring  
946 a few hours before that of N25. This delay in maxima may be caused by a slow particle  
947 growth due to photochemically produced condensable vapors. With a peak around noon  
948 MEV-events show the earliest daily peak occurrence with PCT and DGR-events peaking  
949 between 15 and 17 h, more closely to the maximum solar flux. Considering the diurnal  
950 variation in vertical trajectory displacement, (DZ), the early daily maximum in MEV-  
951 occurrence may be simply controlled by boundary layer dynamics.

952 With the large database of ten years of aerosol data on Mt. Zeppelin enriched by  
953 environmental atmospheric and marine data occurrences, pathways and potential source areas  
954 of different types of new particle formation in the Svalbard region were elucidated by the  
955 present study. More process related information about new particle formation would require



956 dedicated mechanistic experiments with more detailed information on particle precursors,  
957 ultrafine particles, and boundary layer mixing processes. DGR and MEV-types of new  
958 particle formation seem to be more closely related to near-surface processes. Thus, a low-  
959 level site such as the reopened Station Nord, (Nguyen et al., 2016), would be more suitable  
960 for related mechanistic experiments. Station Nord has the additional advantage of being close  
961 to the potential source regions of DGR and MEV-events identified by the present study.

962

963

964 Acknowledgements

965

966 The back trajectories created through the local use of the HYSPLIT model developed,  
967 maintained and generously distributed by the Air Resources Laboratory of NOAA were a  
968 backbone of the present study. We are most grateful for the ceilometer data provided by the  
969 Alfred-Wegener- Institute in Bremerhaven/Potsdam and to NSIDC for their providing daily  
970 Arctic sea ice data. Complementing our own chemical analyses of Mt. Zeppelin filter data  
971 sodium and sulfate results were taken from the EBAS database at the Norwegian Institute for  
972 Air Research (<http://ebas.nilu.no>), for which we are indebted to Anne-Gunn Hjellbrekke and  
973 Wenche Aas. We thank the NASA Ocean Biology Distributed Active Archive Center  
974 (OB.DAAC) for access to MODIS datasets. We are indebted to Yafang Cheng and Zhibin  
975 Wang for providing the algorithm for calculating the condensation sink. MG acknowledges  
976 the receipt of a Beatriu de Pinós post-doctoral fellowship funded by the Generalitat de  
977 Catalunya.

978



- 979 Literature
- 980
- 981 Agarwal, J. K., and Sem, G. J.: Continuous flow, single-particle-counting condensation
- 982 nucleus counter, *J. Aerosol Sci.*, 11, 343-357, 1980.
- 983 An, N., and Wang, K.: A Comparison of MODIS-Derived Cloud Fraction with Surface
- 984 Observations at Five SURFRAD Sites, *J. Appl. Meteor. Clim.*, 54, 1009-1020, 2015.
- 985 Asmi, E., Kondratyev, V., Brus, D., Laurila, T., Lihavainen, H., Backman, J., Vakkari, V.,
- 986 Aurela, M., Hatakka, J., Viisanen, Y., Uttal, T., Ivakhov, V., and Makshtas, A.:
- 987 Aerosol size distribution seasonal characteristics measured in Tiksi, Russian Arctic,
- 988 *Atmos. Chem. Phys.*, 16, 1271-1287, 10.5194/acp-16-1271-2016, 2016.
- 989 Ayers, G. P., Caine, J. M., Granek, H., and Leck, C.: Dimethylsulfide oxidation and the ratio
- 990 of methanesulfonate to non sea-salt sulfate in the marine aerosol, *J. Atmos. Chem.*, 25,
- 991 307-325, 1996.
- 992 Becagli, S., Lazzara, L., Marchese, C., Dayan, U., Ascanius, S. E., Cacciani, M., Caiazza, L.,
- 993 Di Biagio, C., Di Iorio, T., di Sarra, A., Eriksen, P., Fani, F., Giardi, F., Meloni, D.,
- 994 Muscari, G., Pace, G., Severi, M., Traversi, R., and Udisti, R.: Relationships linking
- 995 primary production, sea ice melting, and biogenic aerosol in the Arctic, *Atmos.*
- 996 *Environ.*, 136, 1-15, <http://dx.doi.org/10.1016/j.atmosenv.2016.04.002>, 2016.
- 997 Beine, H. J., Argentini, S., Maurizi, A., Mastrantonio, G., and Viola, A.: The local wind field
- 998 at Ny-Ålesund and the Zeppelin mountain at Svalbard, *Meteorol. Atmos. Phys.*, 78,
- 999 107-113, 2001.
- 1000 Bélanger, S., Babin, M., and Tremblay, J.-É.: Increasing cloudiness in Arctic damps the
- 1001 increase in phytoplankton primary production due to sea ice receding, *Biogeosciences*,
- 1002 doi:10.5194/bg-5110-4087-2013, 2013.
- 1003 Blanchard, D. C., and Woodcock, A. H.: Bubble formation and modification in the sea and its
- 1004 meteorological significance, *Tellus*, 9, 145-158, 1957.
- 1005 Browse, J., Carslaw, K. S., Mann, G. W., Birch, C. E., Arnold, S. R., and Leck, C.: The
- 1006 complex response of Arctic aerosol to sea-ice retreat, *Atmos. Chem. Phys.*, 14, 7543-
- 1007 7557, 10.5194/acp-14-7543-2014, 2014.
- 1008 Charlson, R. J., Lovelock, J. E., Andreae, M. O., and Warren, S. G.: Oceanic phytoplankton,
- 1009 atmospheric sulphur, cloud albedo and climate, *Nature*, 326, 655-661, 1987.
- 1010 Croft, B., Martin, R. V., Leaitch, W. R., Tunved, P., Breider, T. J., D'Andrea, S. D., and
- 1011 Pierce, J. R.: Processes controlling the annual cycle of Arctic aerosol number and size
- 1012 distributions, *Atmos. Chem. Phys.*, 16, 3665-3682, 10.5194/acp-16-3665-2016, 2016a.



- 1013 Croft, B., Wentworth, G. R., Martin, R. V., Leaitch, W. R., Murphy, J. G., Murphy, B. N.,  
1014 Kodros, J. K., Abbatt, J. P. D., and Pierce, J. R.: Contribution of Arctic seabird-colony  
1015 ammonia to atmospheric particles and cloud-albedo radiative effect, *Nature*  
1016 *Communications*, 7, 13444, 10.1038/ncomms13444  
1017 <http://www.nature.com/articles/ncomms13444-supplementary-information>, 2016b.
- 1018 Dal Maso, M., Kulmala, M., Riipinen, I., Wagner, R., Hussein, T., Aalto, P. P., and Lehtinen,  
1019 K. E. J.: Formation and growth of fresh atmospheric aerosols: eight years of aerosol  
1020 size distribution data from SMEAR II, Hyytiälä, Finland, *Bor. Env. Res.*, 10, 323-336,  
1021 2005.
- 1022 Das, R., Granat, L., Leck, C., Praveen, P. S., and Rodhe, H.: Chemical composition of  
1023 rainwater at Maldives Climate Observatory at Hanimaadhoo (MCOH), *Atmos. Chem.*  
1024 *Phys.*, 11, 3743-3755, 10.5194/acp-11-3743-2011, 2011.
- 1025 Dee, D. P., Uppala, S. M., Simmons, A. J., Berrisford, P., Poli, P., Kobayashi, S., and  
1026 Bechtold, P.: The ERA - Interim reanalysis: Configuration and performance of the  
1027 data assimilation system, *Q. J. Roy. Meteorol. Soc.*, 137, 553-597, 2011.
- 1028 Draxler, R., and Rolph, G.: HYSPLIT (HYbrid Single-Particle Lagrangian Integrated  
1029 Trajectory) Model access via NOAA ARL READY, NOAA Air Resources  
1030 Laboratory, Silver Spring, MD, 2003.
- 1031 Flyger, H., and Heidam, N. Z.: Ground level measurements of the summer tropospheric  
1032 aerosol in Northern Greenland, *J. Aerosol Sci.*, 9, 157-168, 1978.
- 1033 Galí, M., Devred, E., Levasseur, M., Royer, S.-J., and Babin, M.: A remote sensing algorithm  
1034 for planktonic dimethylsulfoniopropionate (DMSP) and an analysis of global patterns,  
1035 *Remote Sens. Environ.*, 171, 171-184, <http://dx.doi.org/10.1016/j.rse.2015.10.012>,  
1036 2015.
- 1037 Galí, M., and Simó, R.: A meta - analysis of oceanic DMS and DMSP cycling processes:  
1038 Disentangling the summer paradox, *Global Biochem. Cycles*, 29, 496-515, 2015.
- 1039 Gao, Q., Leck, C., Rauschenberg, C., and Matrai, P. A.: On the chemical dynamics of  
1040 extracellular polysaccharides in the high Arctic surface microlayer, *Ocean Sci.*  
1041 *Discuss.*, 9, 215-259, 2012.
- 1042 Heintzenberg, J., Bischof, W., Odh, S.-Å., and Moberg, B.: An investigation of possible sites  
1043 for a background monitoring station in the European Arctic., International  
1044 Meteorological Institute in Stockholm, Department of Meteorology, Stockholm  
1045 University, Stockholm, Report Nr. AP-22, 74 pp, 1983.



- 1046 Heintzenberg, J., and Larssen, S.: SO<sub>2</sub> and SO<sub>4</sub> in the Arctic: Interpretation of observations at  
1047 three Norwegian Arctic-subArctic stations, *Tellus*, 35B, 255-265, 1983.
- 1048 Heintzenberg, J.: Arctic haze: air pollution in polar regions, *AMBIO*, 18, 50-55, 1989.
- 1049 Heintzenberg, J., and Leck, C.: Seasonal variation of the atmospheric aerosol near the top of  
1050 the marine boundary layer over Spitsbergen related to the Arctic sulphur cycle, *Tellus*,  
1051 46B, 52-67, 1994.
- 1052 Heintzenberg, J., Leck, C., Birmili, W., Wehner, B., Tjernström, M., and Wiedensohler, A.:  
1053 Aerosol number-size distributions during clear and fog periods in the summer high  
1054 Arctic: 1991, 1996, and 2001, *Tellus*, 58B, 41-50, 2006.
- 1055 Heintzenberg, J., Wehner, B., and Birmili, W.: "How to find bananas in the atmospheric  
1056 aerosol" New approach for analyzing atmospheric nucleation and growth events,  
1057 *Tellus B*, 59, 273-282, 2007.
- 1058 Heintzenberg, J.: The aerosol-cloud-climate conundrum, *IJGW*, 4, 219-241, 2012.
- 1059 Heintzenberg, J., Leck, C., and Tunved, P.: Potential source regions and processes of aerosol  
1060 in the summer Arctic, *Atmos. Chem. Phys.*, 15, 6487-6502, 10.5194/acp-15-6487-  
1061 2015, 2015.
- 1062 Held, A., Brooks, I. M., Leck, C., and Tjernström, M.: On the potential contribution of open  
1063 lead particle emissions to the central Arctic aerosol concentration, *Atmos. Chem.*  
1064 *Phys.*, 11, 3093-3105, 10.5194/acp-11-3093-2011, 2011a.
- 1065 Held, A., Orsini, D. A., Vaattovaara, P., Tjernström, M., and Leck, C.: Near-surface profiles  
1066 of aerosol number concentration and temperature over the Arctic Ocean, *Atmos.*  
1067 *Meas. Tech.*, 4, 1603-1616, 2011b.
- 1068 Hubanks, P., Platnick, S., King, M., and Ridgway, B.: MODIS Atmosphere L3 Gridded  
1069 Product Algorithm Theoretical Basis, Document (ATBD) and Users Guide, 2015.
- 1070 Huschke, R. E.: Arctic cloud statistics from "air calibrated" surface weather observations,  
1071 Rand Corporation Memo. RM 6173-PR, 79 pp, 1969.
- 1072 IOCCG: Ocean Colour Remote Sensing in Polar Seas, Report 16, Eds. Babin, M., Arrigo, K.,  
1073 Bélanger, S. and Forget, M.-H., 129 pp, 2015.
- 1074 Jaenicke, R., and Schütz, L.: Arctic aerosols in surface air, *Idöjaras*, 86, 235-241, 1982.
- 1075 Junge, C. E.: Air chemistry and Radioactivity, Academic Press, New York and London, 382  
1076 pp., 1963.
- 1077 Karl, M., Leck, C., Gross, A., and Pirjola, L.: A Study of New Particle Formation in the  
1078 Marine Boundary Layer Over the Central Arctic Ocean using a Flexible



- 1079 Multicomponent Aerosol Dynamic Model, *Tellus*, 64B,  
1080 doi:<http://dx.doi.org/10.3402/tellusb.v3464i3400.17158>, 2012.
- 1081 Karl, M., Leck, C., Coz, E., and Heintzenberg, J.: Marine nanogels as a source of atmospheric  
1082 nanoparticles in the high Arctic, *Geophys. Res. Lett.*, 40, 3738–3743, DOI:  
1083 10.1002/grl.50661, 2013.
- 1084 Keene, W. C., Pszenny, A. A. P., Galloway, J. N., and Hawley, M. E.: Sea-salt corrections  
1085 and interpretation of constituent ratios in marine precipitation, *J. Geophys. Res.*, 91,  
1086 6647-6658, 1986.
- 1087 Keller, M. D., Bellows, W. K., and Guillard, R. R. L.: A survey of dimethylsulfide production  
1088 in 12 classes of marine phytoplankton, in: *Biogenic sulfur in the environment*, edited  
1089 by: E.S. Saltzman, and Cooper, W. J., American Chemical Society, Washington, D,  
1090 167–182, 1989.
- 1091 King, M. D., Platnick, S., Menzel, W. P., Ackerman, S. A., and Hubanks, P. A.: Spatial and  
1092 temporal distribution of clouds observed by MODIS onboard the Terra and Aqua  
1093 satellites, *IEEE Trans. Geosci. Remote Sens.*, 51, 3826–3852, 2013.
- 1094 Knutson, E. O., and Whitby, K. T.: Aerosol classification by electric mobility: apparatus,  
1095 theory, and applications, *J. Aerosol Sci.*, 6, 443-451, 1975a.
- 1096 Knutson, E. O., and Whitby, K. T.: Accurate Measurement of Aerosol Electrical Mobility  
1097 Moments, *J. Aerosol Sci.*, 6, 453-460, 1975b.
- 1098 Kulmala, M., Dal Maso, M., Mäkelä, J. M., Pirjola, L., Väkevä, M., Aalto, P. P.,  
1099 Määkkulainen, P., Hämeri, K., and O'Dowd, C. D.: On the formation, growth and  
1100 composition of nucleation mode particles, *Tellus*, 53B, 479-490, 2001.
- 1101 Kulmala, M., Vehkamäki, H., Petäjä, T., Dal Maso, M., Lauri, A., Kerminen, V.-M., Birmili,  
1102 W., and McMurry, P. H.: Formation and growth rates of ultrafine atmospheric  
1103 particles: a review of observations, *J. Aerosol Sci.*, 35, 143-176, 2004.
- 1104 Lana, A., Simó, R., Vallina, S. M., and Dachs, J.: Re-examination of global emerging patterns  
1105 of ocean DMS concentration, *Biogeochem.*, 110, 173-182, 2012.
- 1106 Lannefors, H., Heintzenberg, J., and Hansson, H.-C.: A comprehensive study of physical and  
1107 chemical parameters of the Arctic summer aerosol; results from the Swedish  
1108 expedition Ymer-80, *Tellus*, 35B, 40-54, 1983.
- 1109 Leck, C., and Persson, C.: The central Arctic Ocean as a source of dimethyl sulfide: Seasonal  
1110 variability in relation to biological activity, *Tellus*, 48B, 156-177, 1996a.



- 1111 Leck, C., and Persson, C.: Seasonal and short-term variability in dimethyl sulfide, sulfur  
1112 dioxide and biogenic sulfur and sea salt aerosol particles in the arctic marine boundary  
1113 layer, during summer and autumn, *Tellus*, 48B, 272-299, 1996b.
- 1114 Leck, C., and Bigg, E. K.: Aerosol production over remote marine areas - A new route,  
1115 *Geophys. Res. Lett.*, 23, 3577-3581, 1999.
- 1116 Leck, C., and Bigg, E. K.: New particle formation of marine biological origin, *Aerosol Sci.*  
1117 *Technol.*, 44, 570-577, 2010.
- 1118 Leck, C., Gao, Q., Mashayekhy Rad, F., and Nilsson, U.: Size-resolved atmospheric  
1119 particulate polysaccharides in the high summer Arctic, *Atmos. Chem. Phys.*, 13,  
1120 12573-12588, 10.5194/acp-13-12573-2013, 2013.
- 1121 Lindsay, R., Wensnahan, M., Schweiger, A., and Zhang, J.: Evaluation of seven different  
1122 atmospheric reanalysis products in the Arctic, *J. Clim.*, 27, 2588-2606, 2014.
- 1123 Liss, P. S., and Merlivat, L.: Air-sea gas exchange rates: Introduction and synthesis, in: *The*  
1124 *Role of Air-Sea Exchange in Geochemical Cycling*, edited by: Buat-Menard, P.,  
1125 Reidel, Norwell, MS, 113-127, 1986.
- 1126 Maritorena, S., Siegel, D. A., and Peterson, A. R.: Optimization of a semianalytical ocean  
1127 color model for global-scale applications, *Appl. Opt.*, 41.15, 2705-2714, 2002.
- 1128 Matrai, P. A., and Vernet, M.: Dynamics of the vernal bloom in the marginal ice zone of the  
1129 Barents Sea: Dimethyl sulfide and dimethylsulfoniopropionate budgets, *Journal of*  
1130 *Geophysical Research: Oceans*, 102, 22965-22979, 10.1029/96JC03870, 1997.
- 1131 Nguyen, Q. T., Glasius, M., Sørensen, L. L., Jensen, B., Skov, H., Birmili, W., Wiedensohler,  
1132 A., Kristensson, A., Nøjgaard, J. K., and Massling, A.: Seasonal variation of  
1133 atmospheric particle number concentrations, new particle formation and atmospheric  
1134 oxidation capacity at the high Arctic site Villum Research Station, Station Nord,  
1135 *Atmos. Chem. Phys.*, 16, 11319-11336, 10.5194/acp-2016-205, 2016.
- 1136 Norman, A. L., Barrie, L. A., Toom-Sauntry, D., Sirois, A., Krouse, H. R., Li, S. M., and  
1137 Sharma, S.: Sources of aerosol sulphate at Alert: Apportionment using stable isotopes,  
1138 *J. Geophys. Res.*, 104, 11619-11631, 1999.
- 1139 Orellana, M. V., Matrai, P. A., Janer, M., and Rauschenberg, C. D.:  
1140 Dimethylsulfoniopropionate storage in *Phaecystis* (Prymnesiophyceae) secretory  
1141 vesicles *J. Phycol.*, 47, 112-117, 10.1111/j.1529-8817.2010.00936.x, 2011a.
- 1142 Orellana, M. V., Matrai, P. A., Leck, C., Rauschenberg, C. D., Lee, A. M., and Coz, E.:  
1143 Marine microgels as a source of cloud condensation nuclei in the high Arctic, *PNAS*,  
1144 108, 13612-13617, 2011b.



- 1145 Pirjola, L., Kulmala, M., Wilck, M., Bischoff, A., Stratmann, F., and Otto, E.: Formation of  
1146 sulphuric acid aerosols and cloud condensation nuclei: An expression for significant  
1147 nucleation and model comparison, *J. Aerosol Sci.*, 30, 1079-1094, 1999.
- 1148 Polissar, A. V., Hopke, P. K., Paatero, P., Kaufman, Y. J., Hall, D. K., Bodhaine, B. A.,  
1149 Dutton, E. G., and Harris, J. M.: The aerosol at Barrow, Alaska: long-term trends and  
1150 source locations, *Atmos. Environ.*, 33, 2441-2458, 1999.
- 1151 Rahn, K. A., and Shaw, G. E.: Particulate air pollution in the Arctic: Large-scale occurrence  
1152 and meteorological controls, in: *Atmospheric Aerosols and Nuclei*, edited by: Roddy,  
1153 F., and O'Connor, T. C., Dept. of Physics, University College, Galway, Ireland 21-27  
1154 Sept., 223-227, 1977.
- 1155 Rudels, B., Björk, G., Nilsson, J., Winsor, P., Lake, I., and Nohr, C.: The interaction between  
1156 waters from the Arctic Ocean and the Nordic Seas north of Fram Strait and along the  
1157 East Greenland Current: results from the Arctic Ocean-02 Oden expedition, *Journal of*  
1158 *Marine Systems*, 55, 1-30, 2005.
- 1159 Schmidtko, S., Johnson, G. C., and Lyman, J. M.: MIMOC: A global monthly isopycnal  
1160 upper-ocean climatology with mixed layers, *Journal of Geophysical Research:*  
1161 *Oceans*, 118, 1658-1672, 10.1002/jgrc.20122, 2013.
- 1162 Schoemann, V., Becquevort, S., Stefels, J., Rousseau, V., and Lancelot, C.: Phaeocystis  
1163 blooms in the global ocean and their controlling mechanisms: a review, *Journal of Sea*  
1164 *Research*, 53, 43-66, <http://dx.doi.org/10.1016/j.seares.2004.01.008>, 2005.
- 1165 Sharma, S., Chan, E., Ishizawa, M., Toom-Saunty, D., Gong, S. L., Li, S. M., Tarasick, D.  
1166 W., Leaitch, W. R., Norman, A., Quinn, P. K., Bates, T. S., Lefebvre, M., Barrie, L.  
1167 A., and Maenhaut, W.: Influence of transport and ocean ice extent on biogenic aerosol  
1168 sulfur in the Arctic atmosphere, *J. Geophys. Res.*, 117, D12209,  
1169 10.1029/2011JD017074, 2012.
- 1170 Simó, R.: Production of atmospheric sulfur by oceanic plankton: biogeochemical, ecological  
1171 and evolutionary links, *Trends in Ecology & Evolution*, 16, 287-294, 2001.
- 1172 Ström, J., Engvall, A.-C., Delbart, F., Krejci, R., and Treffeisen, R.: On small particles in the  
1173 Arctic summer boundary layer: observations at two different heights near Ny-Ålesund,  
1174 Svalbard, *Tellus B - Chemical and Physical Meteorology*, 61, 473-482, 2009.
- 1175 Tunved, P., Ström, J., and Krejci, R.: Arctic aerosol life cycle: linking aerosol size  
1176 distributions observed between 2000 and 2010 with air mass transport and  
1177 precipitation at Zeppelin station, Ny-Ålesund, Svalbard, *Atmos. Chem. Phys.*, 13,  
1178 3643-3660, 10.5194/acpd-12-29967-2012, 2013.



- 1179 Warren, S. G., and Hahn, C. J.: Cloud climatology, in: Encyclopedia of Atmospheric  
1180 Sciences, edited by: Holton, J. R., Pyle, J., and Curry, J. A., Academic Press, London,  
1181 UK, 476-483, 2002.
- 1182 Wiedensohler, A., Covert, D., Swietlicki, E., Aalto, P., Heintzenberg, J., and Leck, C.:  
1183 Occurrence of an ultrafine particle mode less than 20 nm in diameter in the marine  
1184 boundary layer of the Arctic summer and autumn, *Tellus*, 48B, 213-222, 1996.
- 1185 Willis, M. D., Burkart, J., Thomas, J. L., Köllner, F., Schneider, J., Bozem, H., Hoor, P. M.,  
1186 Aliabadi, A. A., Schulz, H., Herber, A. B., Leitch, W. R., and Abbatt, J. P. D.:  
1187 Growth of nucleation mode particles in the summertime Arctic: a case study, *Atmos.*  
1188 *Chem. Phys. Discuss.*, 2016, 1-31, 10.5194/acp-2016-256, 2016.
- 1189 Zhang, M., Chen, L., Xu, G., Lin, Q., and Liang, M.: Linking Phytoplankton Activity in  
1190 Polynyas and Sulfur Aerosols over Zhongshan Station, East Antarctica, *J. Atmos. Sci.*,  
1191 72, 4629-4642, 2015.
- 1192
- 1193
- 1194



1195

Parameter	TR (h)	Explanation
C25	1 min	25% percentile of cloud base from AWI ceilometer (m)
CF12, 24, 36, 48, 5D	24	Average MODIS cloud fraction during the last 12h, 24h, 36, 48h, and days 3-5 before trajectory arrival
D50	1	Number-median diameter of particles < 50 nm diameter
CS	1	Condensation sink ( $s^{-1}$ )
DZ	1	Vertical trajectory displacement ( $m h^{-1}$ ) during the last hour before arrival
MSA	$\geq 1$ day	Methane sulfonate ( $nmol m^{-3}$ )
N10	1	Number concentration of particles up to 10 nm ( $>2010, cm^{-3}$ )
N20	1	Number concentration between 10 and 20 nm ( $cm^{-3}$ )
N25	1	Number concentration of particles up to 25 nm ( $cm^{-3}$ )
N40	1	Number concentration between 20 and 40 nm ( $cm^{-3}$ )
N60	1	Number concentration between 40 and 60 nm ( $cm^{-3}$ )
N100	1	Number concentration between 60 and 100 nm ( $cm^{-3}$ )
N300	1	Number concentration between 100 and 300 nm ( $cm^{-3}$ )
Na	$\geq 1$ day	Sodium concentrations ( $nmol m^{-3}$ )
NCO	1	Number concentration of particles > 300 nm ( $cm^{-3}$ )
nssSO <sub>4</sub> <sup>2-</sup>	$\geq 1$ day	Non-sea salt sulfate concentrations ( $nmol m^{-3}$ )
NTO	1	Number concentration of particles $\geq 10$ nm, ( $cm^{-3}$ )
OC12, 24, 36, 48, 5D	120	Average MODIS DMSPt (nmol) during the last 12h, 24h, 36, 48h, and days 3-5 before trajectory arrival
OW12, 24, 36, 48, 5D	24	Average open water (%) during the last 12h, 24h, 36, 48h, and days 3-5 before trajectory arrival
PRE	1	Trajectory precipitation (mm) at arrival
RH	1	Trajectory relative humidity (%) at arrival
SFL	1	Solar flux at trajectory arrival ( $W m^{-2}$ )
SP12, 24, 36, 48, 5D	1	Accumulated precipitation (mm) during the last 12h, 24h, 36, 48h, and days 3-5 before trajectory arrival
T12, 24, 36, 48, 5D	24	Average sea surface temperature (C) during the last 12h, 24h, 36, 48h, and days 3-5 before trajectory arrival
TEM	1	Trajectory temperature (C) at arrival
WDR	1	Trajectory wind direction ( $^{\circ}$ ) during the last hour before arrival
WSP	1	Trajectory wind speed ( $m sec^{-1}$ ) during the last hour before arrival

1196

1197 Table 1 Aerosol, atmospheric, and ocean parameters utilized in the present study.

1198 DMSPt = Total dimethylsulfoniopropionate in surface ocean waters. TR = temporal

1199 resolution in which the respective data were available.

1200

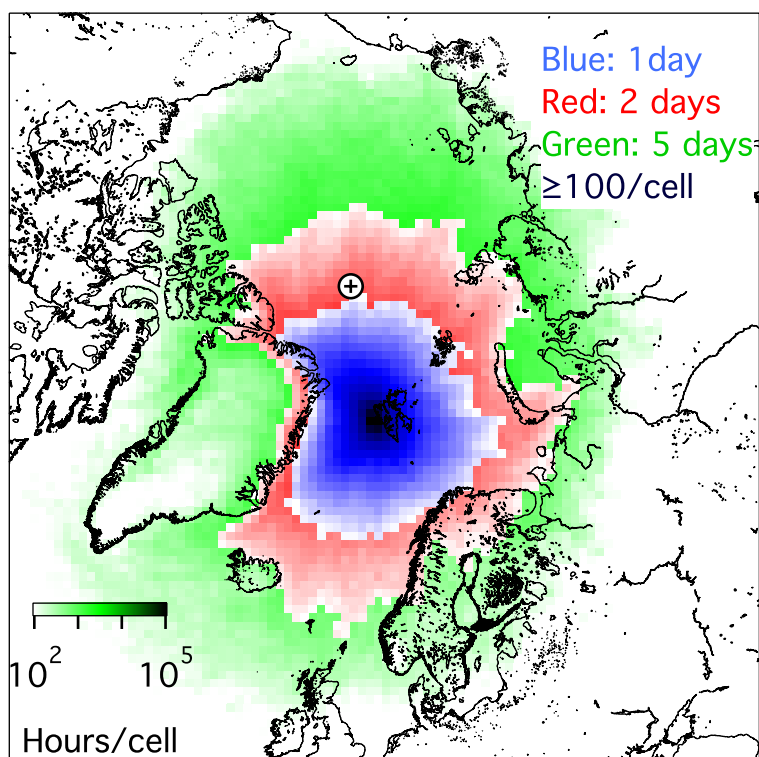


1201  
1202  
1203  
1204  
1205  
1206  
1207  
1208

<b>Approach</b>	<b>Acronym</b>	<b>Criteria and thresholds</b>	<b>Total number of events</b>	<b>Number of unique events</b>
Percentiles	PCT	N25 >93%-percentile	4143	240
Diameter-growth	DGR	D50-Growth >1.5	1199	235
Multi-size growth	MEV	Multi-growth >1.6	1191	266
Sum			6533	741

1209  
1210  
1211  
1212

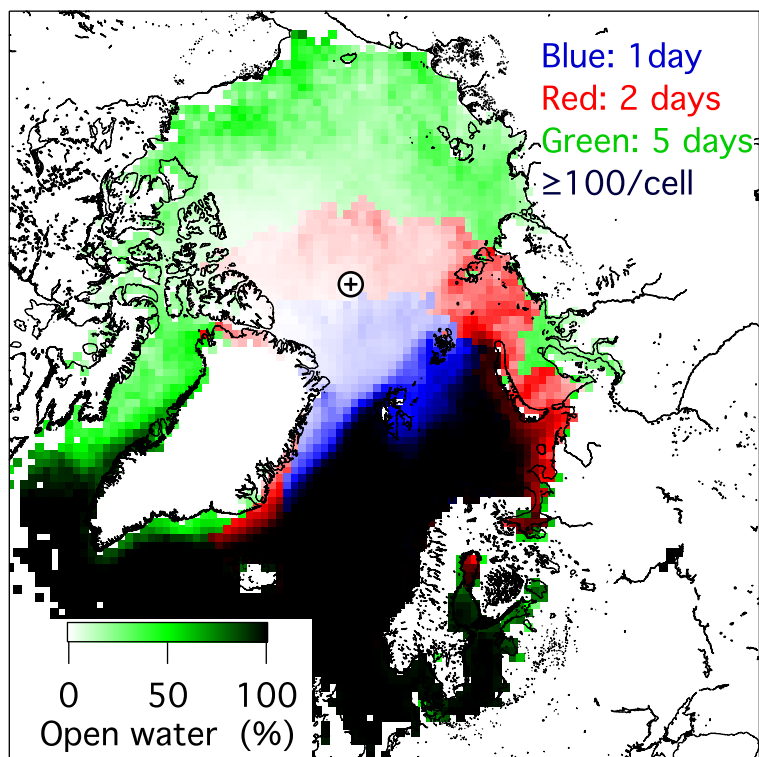
Table 2 Total and unique number of events of new particle formation identified by the three approaches to identify NPF-events.



1213

1214 Fig. 1 Map of the regional distribution of 5-day (green), 2-day (red), and 1-day (blue)  
1215 hourly back trajectories to Mt. Zeppelin during the months March through October  
1216 of the years 2006 - 2015. Black symbol: North Pole. The colored areas are covered  
1217 with at least 100 trajectory hours per geocell and the color saturation corresponds to  
1218 the number of trajectory hours per grid cell on a log-scale.

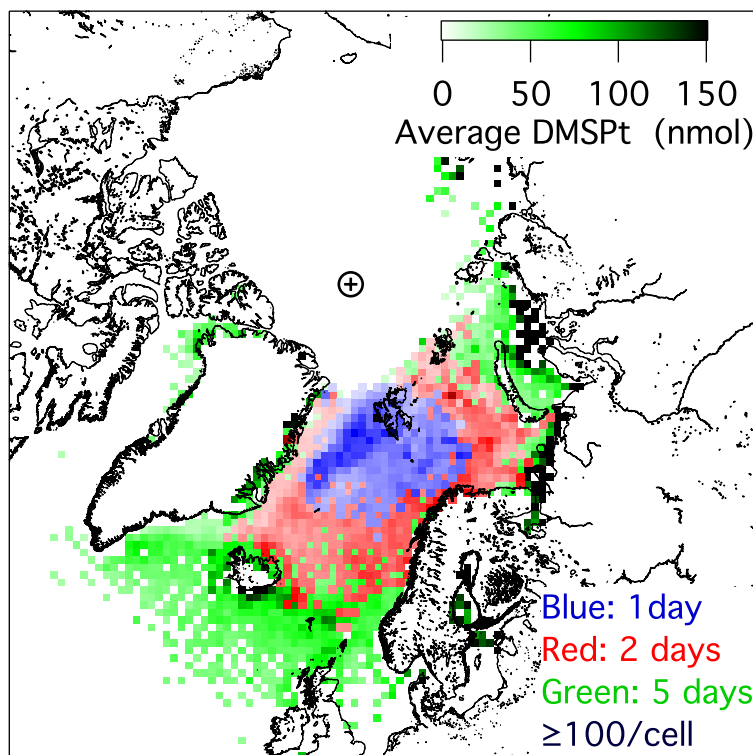
1219



1220

1221 Fig. 2 Map of the regional distribution of open water under 87648 5-day (green), 2-day  
1222 (red), and 1-day (blue) hourly back trajectories to Mt. Zeppelin during the during the  
1223 months March through October of the years 2006-2015. Black symbol: North Pole.  
1224 The areas are covered with at least 100 trajectory hours concurrent with data values  
1225 per geocell.

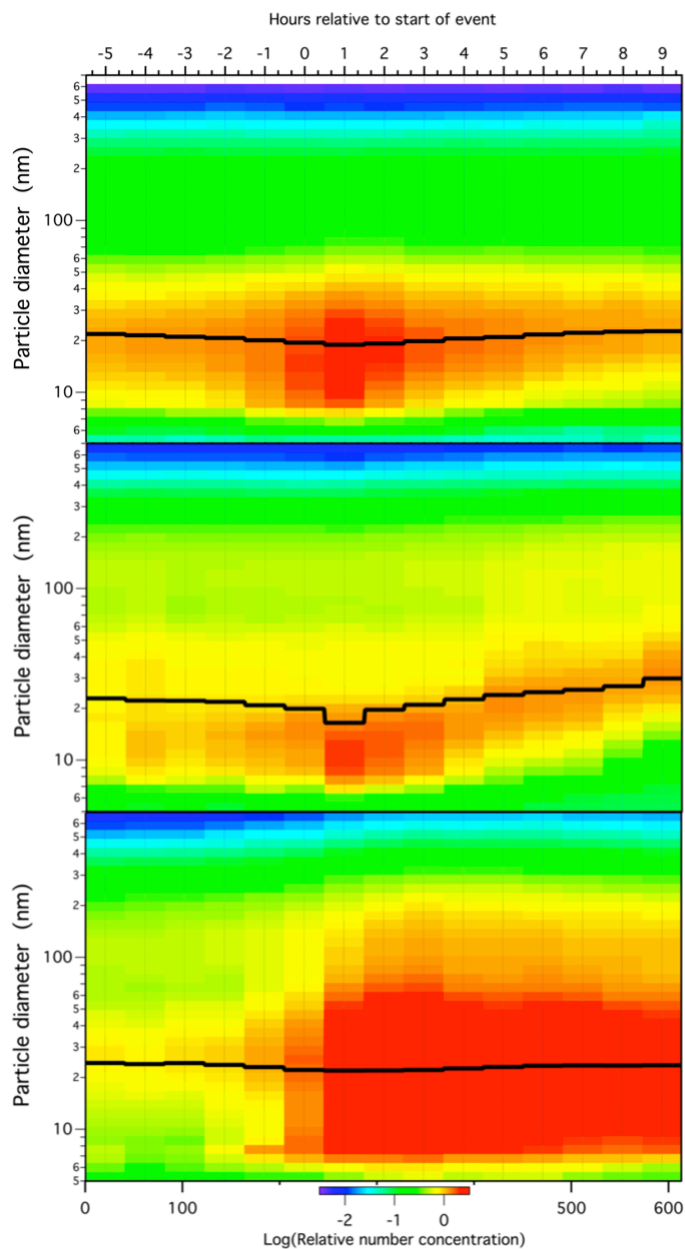
1226



1227

1228 Fig. 3 Map of the regional distribution of DMSPt along 87648 5-day (green), 2-day (red),  
1229 and 1-day (blue) hourly back trajectories to Mt. Zeppelin during the during the  
1230 months March through October of the years 2006-2015. Black symbol: North Pole.  
1231 The relative color scale holds for all colors. The areas are covered with at least 100  
1232 trajectory hours with data values per geocell.

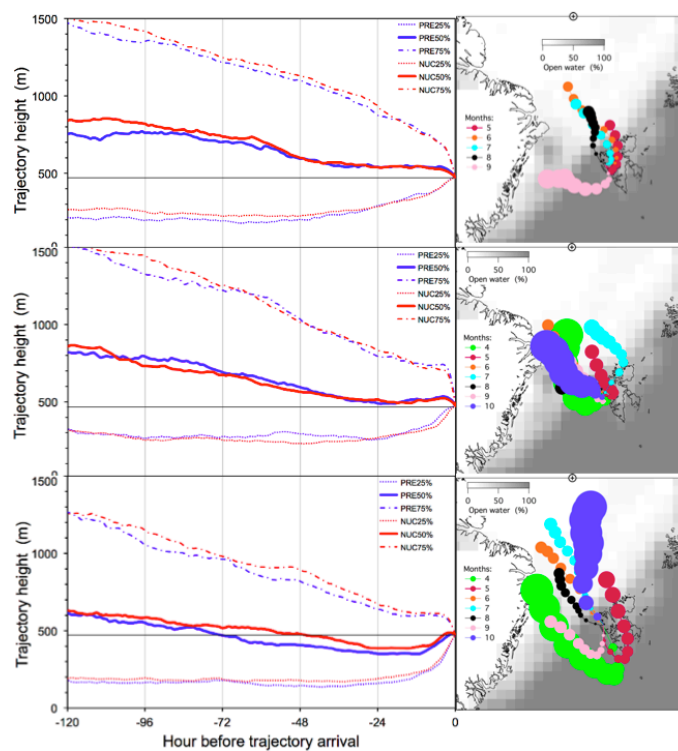
1233



1234

1235 Fig.4 Average temporal development of the relative number size distribution before and  
1236 during NPF-events identified by the three approaches. The black curve gives the  
1237 median sub-50-nm particle diameter D50 during the events. Top: PCT-events;  
1238 center: DGR-events; bottom: MEV-events.

1239

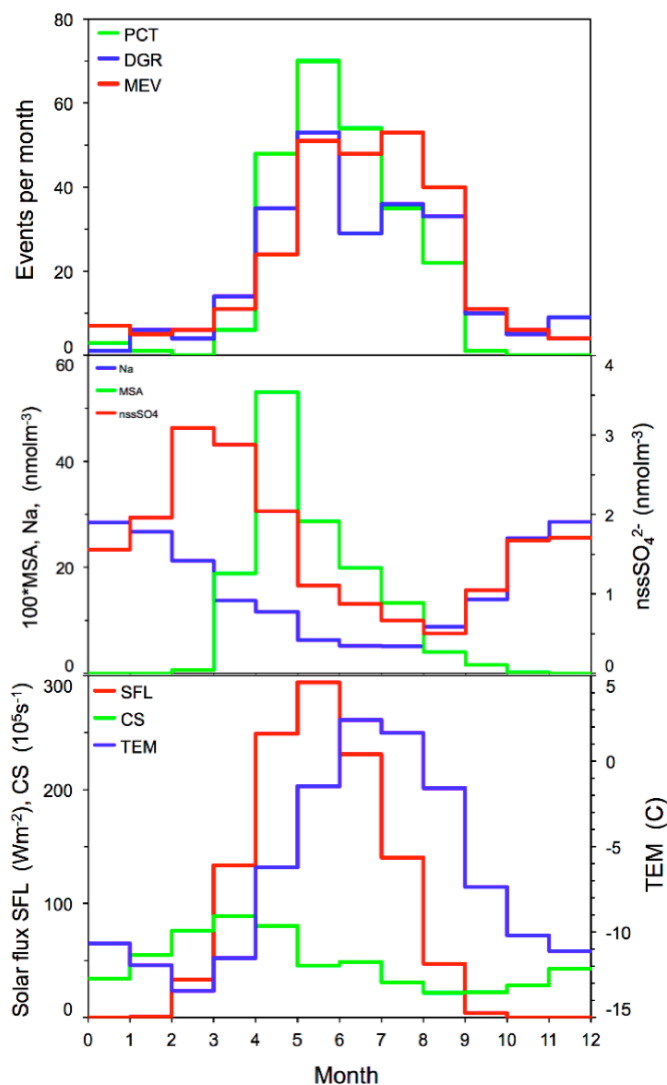


1240

1241 Fig. 5 Left panels: Median back trajectory height profiles (m) during the six pre-event  
1242 hours (full line in blue, PRENUC) and during the nine DGR-event hours (full line in  
1243 red, NUC). 25% and 75% percentiles are shown as dotted, and dash-dotted lines,  
1244 respectively. Top: PCT-events; center: DGR-events; bottom: MEV-events. The thin  
1245 horizontal line marks the station level.

1246 Right panels: Average monthly trajectory positions in 12 h steps for the months April  
1247 though October. Only months with at least 10 NPF-events are shown. The circles  
1248 comprise 95% of all trajectories at any trajectory step. The underlying grey-scale  
1249 map indicates July ice cover averaged over the years 2006 – 2015

1250



1251

1252 Fig. 6 Top: Monthly numbers of new particle formation events according to the three  
1253 approaches. PCT: Upper percentile of N25; DGR: Diameter growth; MEV: Multiple  
1254 size events.

1255 Center: Average seasonal distribution of particle composition in  $\text{nmolm}^{-3}$ .

1256 Na = sodium,  $\text{nssSO}_4 = \text{nssSO}_4^{2-}$ , MSA = Methane sulfonate times 100.

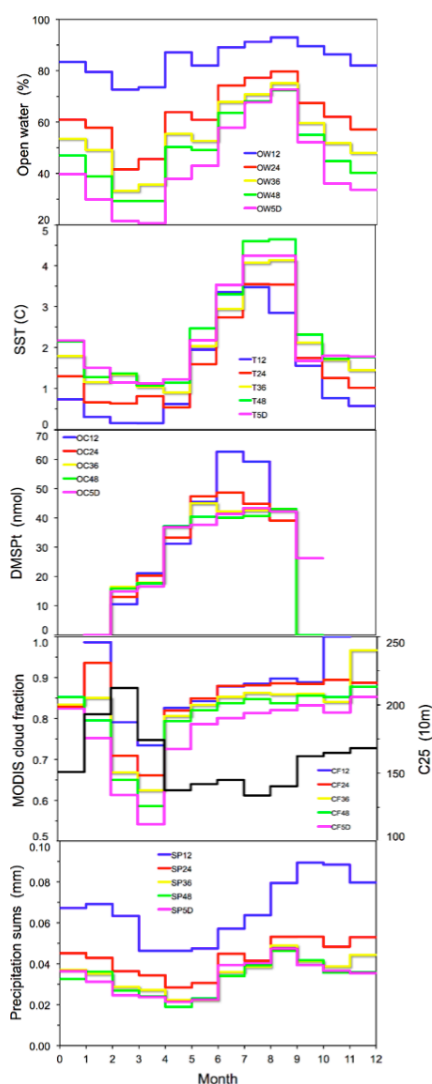
1257 Bottom: Monthly average solar flux (SFL, red,  $\text{Wm}^{-2}$ ), and temperature (TEM, blue

1258  $^{\circ}\text{C}$ ), and condensation sink, (CS,  $10^5\text{s}^{-1}$ ), at Mt. Zeppelin, Spitsbergen.

1259



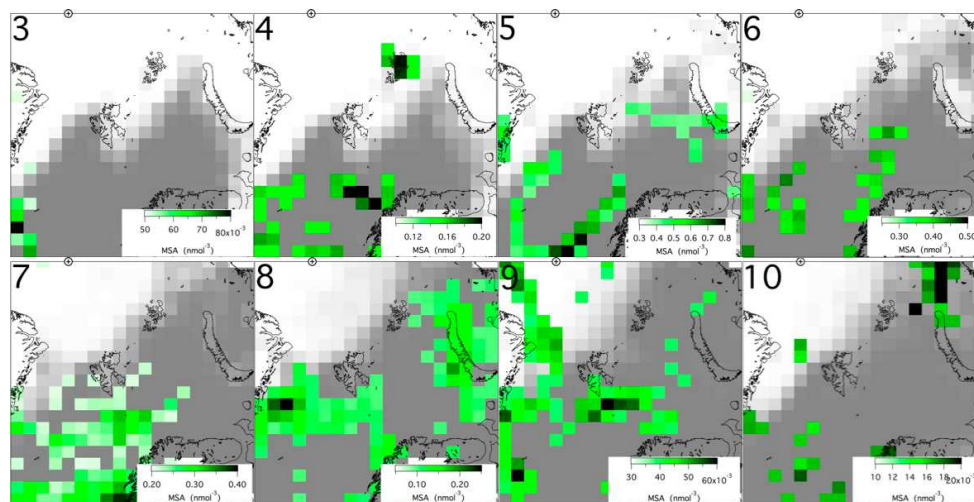
1260



1261

1262 Fig. 7 Monthly averages of environmental parameters averaged along back trajectories to  
1263 Mt. Zeppelin. From top to bottom: OW12-5D: Open water in % during last 12, 24,  
1264 36, and 48h, and days 3-5 before trajectory arrival at Mt. Zeppelin. T12-5D: Same  
1265 for sea surface temperature in °C. OC12-5D: Same for DMSPt in nmol in surface  
1266 waters. CF12-5D: Same for MODIS cloud fraction. SP12-5D: Same for  
1267 precipitation sums in mm. C25 = 25%-percentile of cloud base in decameter.

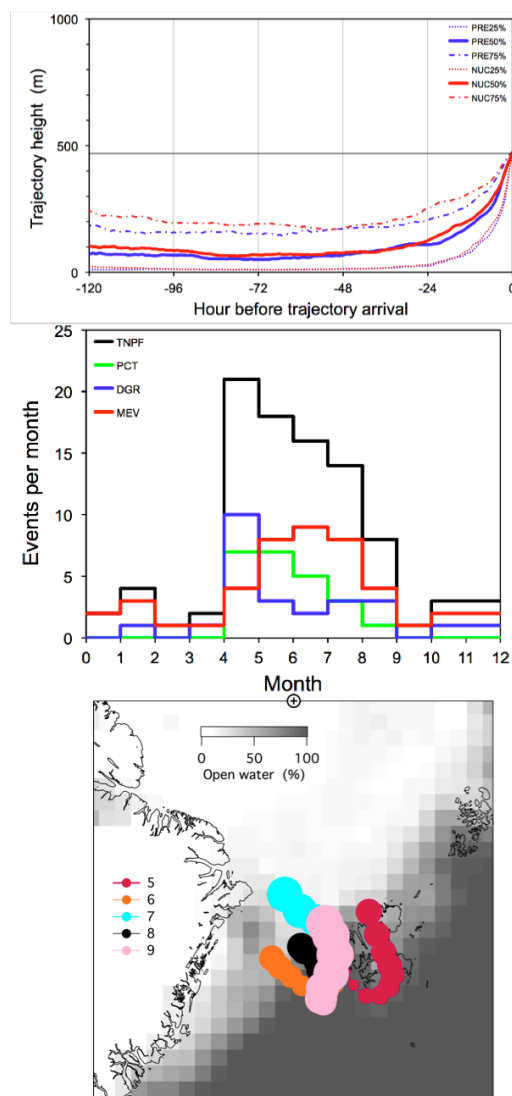
1268



1269

1270 Fig. 8 Average monthly distribution of methane sulfonic acid, (MSA,  $\text{nmol m}^{-3}$ ), during the  
1271 months March – October of the years 2006 – 2015, constructed from MSA-  
1272 concentrations measured on Mt. Zeppelin, which were extrapolated along 5-day back  
1273 trajectories. Average open water percentages during the respective months are  
1274 indicated as white (0% open water) to dark grey (100% open water) areas. The  
1275 position of the North Pole is marked as cross in circle on the upper border of the  
1276 maps.

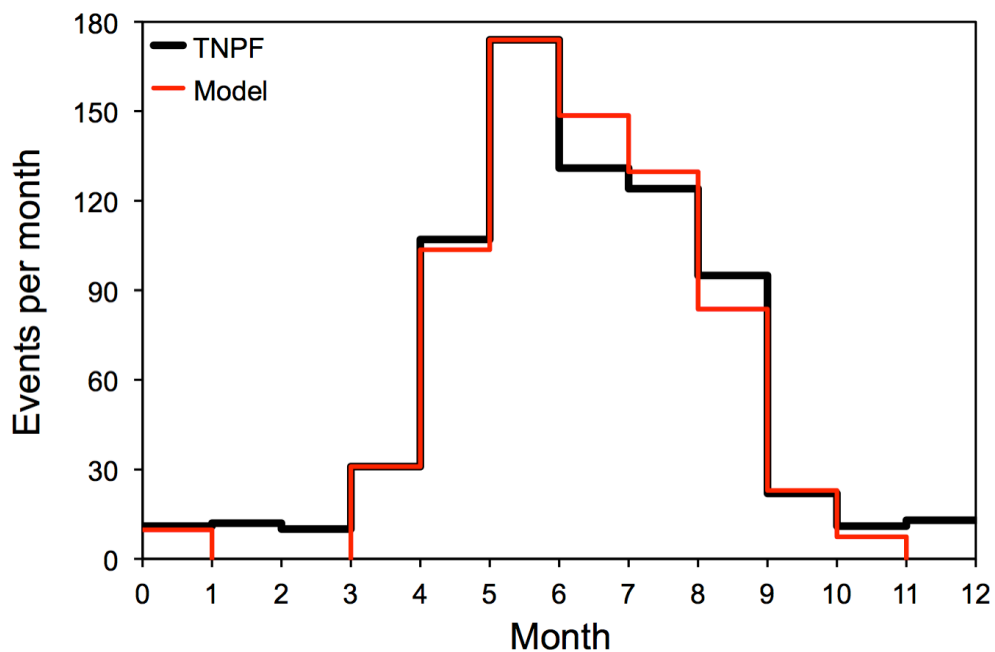
1277



1278

1279 Fig. 9 Characteristics of the subpopulation of 93 NPF-events with back trajectories that  
1280 stayed below 500 m for five days before arrival. Top: Statistics of related vertical  
1281 trajectory coordinates as in Fig. 5. Center: Average monthly occurrence of PCT,  
1282 DGR, and MEV-events. Bottom: Related average monthly trajectory positions in  
1283 12 h steps for the months May through September. The circles comprise 95% of all  
1284 trajectories at any trajectory step. The underlying grey-scale map indicates July ice  
1285 cover averaged over 2006 – 2015.

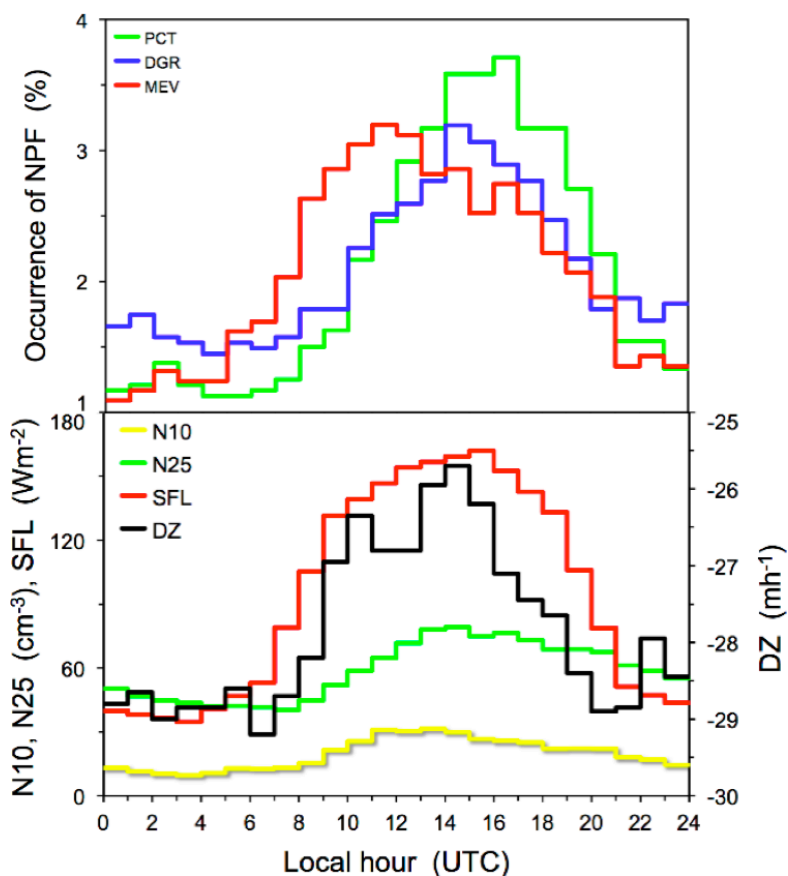
1286



1287

1288 Fig. 10 Average monthly sums of NPF-events due to the three types of new particle  
1289 formation, (TNPF, black). Red: Three-parameter model to describe TNPF.

1290



1291

1292 Fig. 11 Top: Relative average diurnal occurrence of the three types NPF-events. PCT:

1293 Upper percentile of N25; DGR: Diameter growth; MEV: Multiple size events.

1294 Bottom: Average diurnal variation of the HYSPLIT-modeled solar flux (SFL,  $\text{Wm}^{-2}$ ),

1295 the integral particle concentrations N10, and N25 in  $\text{cm}^{-3}$ , and of the vertical

1296 displacement parameter (DZ,  $\text{mh}^{-1}$ ). N10 is based on data of the years 2011 – 2015

1297 whereas the other parameters are based on data of the years 2006 – 2015.